NeuroImage 201 (2019) 116007

Contents lists available at ScienceDirect

NeuroImage

journal homepage: www.elsevier.com/locate/neuroimage

Network analysis of whole-brain fMRI dynamics: A new framework based on dynamic communicability

Matthieu Gilson [a,*], Nikos E. Kouvaris [b,e], Gustavo Deco [a,c], Jean-François Mangin [d], Cyril Poupon [d], Sandrine Lefranc [d], Denis Rivière [d], Gorka Zamora-López [a]

[a] Center for Brain and Cognition, Computational Neuroscience Group, Department of Information and Communication Technologies, Universitat Pompeu Fabra, Carrer de Ramon Trias Fargas 25-27, Barcelona, 08005, Spain
[b] Namur Institute for Complex Systems (naXys), Department of Mathematics, University of Namur, Rempart de la Vierge 8, B 5000, Namur, Belgium
[c] Institució Catalana de la Recerca i Estudis Avançats (ICREA), Universitat Pompeu Fabra, Passeig Lluís Companys 23, Barcelona, 08010, Spain
[d] Neurospin, CEA, Paris Saclay University, Gif-sur-Yvette, 91191, France
[e] DRIBIA Data Research S.L., Barcelona, Spain

A B S T R A C T

Neuroimaging techniques such as MRI have been widely used to explore the associations between brain areas. Structural connectivity (SC) captures the anatomical pathways across the brain and functional connectivity (FC) measures the correlation between the activity of brain regions. These connectivity measures have been much studied using network theory in order to uncover the distributed organization of brain structures, in particular FC for task-specific brain communication. However, the application of network theory to study FC matrices is often "static" despite the dynamic nature of time series obtained from fMRI. The present study aims to overcome this limitation by introducing a network-oriented analysis applied to whole-brain effective connectivity (EC) useful to interpret the brain dynamics. Technically, we tune a multivariate Ornstein-Uhlenbeck (MOU) process to reproduce the statistics of the whole-brain resting-state fMRI signals, which provides estimates for MOU-EC as well as input properties (similar to local excitabilities). The network analysis is then based on the Green function (or network impulse response) that describes the interactions between nodes across time for the estimated dynamics. This model-based approach provides time-dependent graph-like descriptor, named communicability, that characterize the roles that either nodes or connections play in the propagation of activity within the network. They can be used at both global and local levels, and also enables the comparison of estimates from real data with surrogates (e.g. random network or ring lattice). In contrast to classical graph approaches to study SC or FC, our framework stresses the importance of taking the temporal aspect of fMRI signals into account. Our results show a merging of functional communities over time, moving from segregated to global integration of the network activity. Our formalism sets a solid ground for the analysis and interpretation of fMRI data, including task-evoked activity.

1. Introduction

The study of brain connectivity, or connectome, has attracted much attention in the recent years to interpret measurements from structural and functional magnetic resonance imaging, respectively sMRI and fMRI; for a review see (Sporns, 2013). Functional connectivity (FC) measures the correlation structure of the observed fMRI/BOLD activity and has been used as a proxy for interactions between brain regions (Goense et al., 2012). Structural connectivity (SC) describes the architecture of anatomical fibers between brain regions and hints at possible pathways for neuronal communication (Sporns et al., 2000). Tools from network theory have been applied to SC and FC to investigate how distributed brain functions operate. The power of network-oriented analyses is the quantification of how distant brain regions "communicate", e.g. in the sense of being connected or exchanging information. For example, the 'global workspace theory' postulates that the information processed in parallel by separate sensory systems is integrated by some high-level brain regions (Baars, 1988, 2002), which has been experimentally tested with conscious access of stimuli (Dehaene and Naccache, 2001; Schröter et al., 2012). This hypothesis is supported by the observations that SC and FC exhibit a complex organization involving modules linked by hubs that centralize the cross-modular communications in a small-world manner (Zamora-López et al., 2009; van den Heuvel et al., 2012). This leads to the concepts of segregation within modules and integration between them (Tononi et al., 1994).

In this paper we introduce a new formalism to study functional brain connectivity that goes beyond the "static" graph analysis of FC. To do so, the key is the use of a dynamic network model for the propagation of brain activity, which is fitted to the fMRI data (and also incorporates information from SC). In *dynamic communicability* the interaction from a

* Corresponding author. Universitat Pompeu Fabra, C/ Ramon de Trias Fargas, 25-27, Barcelona, 08005, Spain.
E-mail address: matthieu.gilson@upf.edu (M. Gilson).

https://doi.org/10.1016/j.neuroimage.2019.116007
Received 27 January 2019; Received in revised form 4 June 2019; Accepted 9 July 2019
Available online 12 July 2019

source node to a target node is defined as the activity reaching the target via the network after a unit perturbation at the source, as evaluated in the tuned model (Gilson et al., 2018). This allows for the definition of a variety of graph measures to quantify the *spatio-temporal* organization of network interactions, from early to late times after the perturbation. A fundamental advantage of our framework is that we make the same assumptions from connectivity estimation to network descriptors and their interpretation. We also stress that this approach is model agnostic, in the sense that any dynamic network model can be used provided its Green function (or impulse response function) is known (Gilson et al., 2018). We now focus on three important novelties about our approach compared to previous work.

A particular issue concerns weighted networks that naturally arise in brain network models —as well as in brain connectivity. SC and FC have been extensively investigated as complex networks using the statistical descriptors provided by graph theory, which were originally defined for undirected and unweighted networks (Albert and Barabási, 2002; Barrat et al., 2004; Bang-Jensen and Gutin, 2009). In other words, graph measures are often applied in an "off-the-shelf" manner, which limits the potential of the data interpretation. As an (extreme) example, small-worldness relies on paths in a binary graph and its application to a thresholded-binarized version of FC appears inappropriate, as the FC "weights" represent statistical dependencies that fundamentally differ from paths. *Graph communicability* is a notable effort to extend graph analysis to weighted networks, naturally incorporating the heterogeneity of link weights in the graph measures (Estrada and Hatano, 2008). In essence, it evaluates the "influence" that a node exerts over another by taking into account indirect paths —not only shortest paths— which is important to take global effects in recurrently-connected networks (Andreotti et al., 2014). Graph communicability has been used to describe nodes as listeners or broadcasters in networks (Estrada, 2013). Likewise, centrality measures defined from graph communicability transpose the notion of short paths for small-worldness to influence between nodes due to all possible indirect paths (Benzi and Klymko, 2013; Arrigo and Benzi, 2016). In the context of neuroimaging, graph communicability was employed to show the limited contribution of SC topology to explain the empirically observed FC (Bettinardi et al., 2017).

A shortcoming of graph communicability is that its underlying dynamical model only gives rise to divergent behavior, which led us to introduce *dynamic communicability* for stable dynamics (Gilson et al., 2018). This is important when considering BOLD signals, whose temporal structure has recently raised much interest (He, 2011; Hutchison et al., 2013; Mitra et al., 2015). Among previous approaches to incorporate time in BOLD analysis, the 'dynamic FC' uses sliding time windows over which FC matrices are computed, focusing on the statistical dependences between ROIs at the timescale of a minute (Hutchison et al., 2013). The successive FC matrices can be clustered to define "states" for the whole network at different temporal snapshots (Khambhati et al., 2018; Thompson et al., 2017; Avena-Koenigsberger et al., 2017; Nielsen et al., 2018). Another recent study relies on hidden Markov models (HMMs) to generate BOLD activity and study the transition between states defined at the shorter timescale of a few seconds (Vidaurre et al., 2018). However, such studies assume the successive time points of BOLD activity to be independent snapshots corrupted by noise, without considering the propagating nature of the BOLD signals. We lift this limitation by using a model that captures the BOLD time-lagged correlations in its tuned directed connectivity.

Early definitions of integration relied on the mutual information or the cross-correlation between the observed activity of subgroups of nodes in the network (Tononi et al., 1994; Barnett et al., 2009). Following, network-oriented analyses applied on data or network models have sought collective patterns to quantify integration in the model activity, e.g. via the dynamic FC to take time into account (Fair et al., 2007; Deco et al., 2015; Fransson et al., 2018). However, it can be argued that these integration measures focus on the observed or generated activity rather than on their causes. The complexity of the network activity does reflect the interplay between hubs and network motifs such as modules (Galán, 2008; Senden et al., 2014; Zamora-López et al., 2016). In a previous study we applied network theory to the model connectivity (Senden et al., 2018; Gilson et al., 2018b). In contrast, we use the Green function as the basis for information processing in our model-based approach.

Given the novelties mentioned above (dynamic communicability in a model-based approach), this paper provides a concrete implementation that is consistent from estimation to interpretation of data. We use the multivariate Ornstein-Uhlenbeck (MOU) process as a generative model for the BOLD signals in order to extract whole-brain effective connectivity —referred to as MOU-EC (Gilson et al., 2016, 2018b). The estimated MOU-EC has been demonstrated to be a robust signature for the prediction of subject identity and task performed by them (Pallarés et al., 2018). Note that the MOU process captures the observed BOLD dynamics; Instead, other models like dynamic causal model (DCM) focus on the neuronal dynamics by incorporating a hemodynamic response (Friston, 2011; Frässle et al., 2017; Razi et al., 2017). The MOU model has also been used in the initial framework of dynamic communicability, since its Green function is analytically tractable (Gilson et al., 2018). After summarizing important points concerning the MOU-EC estimation from BOLD signals (Gilson et al., 2016), the Methods section introduces the novel formalism of dynamic communicability to analyze complex network dynamics with linear coupling (Gilson et al., 2018). In the Results section we apply it to resting-state fMRI and diffusion MRI of the ARCHI database acquired by the European project Connect (Assaf et al., 2013; Duclap et al., 2013) and available at the NeuroInformatics Platfrom of the Human Brain Project. We show how dynamic communicability provides a finer and more general description of the network dynamics than classical analysis based on FC or SC, while focusing on the temporal aspect of our formalism. In particular, we examine several aspects of integration like the listening or broadcasting roles of ROIs to the rest of the network. In addition, we identify the early (local) to late (global) organization of the activity propagation in the network following stimulation.

2. Methods

2.1. Resting-state fMRI time series and structural connectomes

The analyses were applied to the ARCHI database (Assaf et al., 2013; Duclap et al., 2013) composed of 77 subjects (32 females, mean age 23.65 years, with standard deviation 5.16) with high quality T1-weighted images and diffusion data acquired on a Magnetom TimTrio 3T MRI System (Siemens Healthcare, Erlangen, Germany). The MRI protocol included:

- a T1-weighted MRI scan using a MPRAGE pulse sequence with the following settings: field of view FOV = 256 mm, flip angle FA = 9°, inversion time TI = 900 ms, echo time TE = 2.98 ms, repetition time TR = 2300 ms, 160 slices, slice thickness TH = 1.1 mm, in-plane matrix 256 × 256, read bandwidth RBW = 240 Hz/pixel;
- a calibration fieldmap scan using a double gradient echo 2D pulse sequence with the following parameters: FOV = 220 mm, FA = 60°, echo times TE1/TE2 = 4.92/7.38 ms, TR = 500 ms, 35 slices, TH = 3.5 mm, in-plane matrix 64 × 64, RBW = 200 Hz/pixel;
- a resting-state fMRI scan using a 2D gradient-echo echoplanar pulse (GRE EPI) sequence with the following parameters: FOV = 192 mm, FA = 81°, TE = 30 ms, TR = 2400 ms, 40 slices, TH = 3.0 mm, in-plane matrix 64 × 64, RBW = 2442 Hz/pixel, no parallel imaging option, partial Fourier factor = 1.0; each session has 244 frames for a total scan time of 9 min 46 s.

The T1-weighted structural MRI data was processed using Freesurfer 5.3 software (Fischl et al., 1999), which performed cortical tissue (gray and white matters) segmentation, and built surface meshes for both pial interface and grey/white interface of each hemisphere. Surface

alignment was performed to an inter-subject template, allowing the projection of the Desikan atlas on these anatomical meshes (Desikan et al., 2006). The fMRI final activity was obtained by averaging the BOLD signals projected on each mesh vertex over each ROI of the Desikan atlas, see Table 1 below.

Individual SC matrices were built using Diffusion weight imaging (DWI) following the processing steps of the Connectomist-2.0 software (Duclap et al., 2012): artifact correction, geometrical distortion correction, analytical Q-ball model (Descoteaux et al., 2007), streamline probabilistic fiber tracking inside an improved T1-based brain mask (Guevara et al., 2011) using 27 seeds per voxel at the T1 image resolution and propagation step size of 0.4 mm. Unreliable short fibers under 30 mm were removed, then region-to-region SC matrices could be built by counting fibers connecting regions of a given atlas (Lefranc et al., 2016). From the individual SC matrices, we calculated a generic SC matrix by averaging over all subjects.

The Constellation parcellation is a refinement from the Freesurfer parcellation based on the DTI data. It subdivides each Freesurfer ROI according to the structural connectivity profile of each ROI point such as to obtain 3 to 5 Constellation ROIs with increased SC homogeneity (Lefranc et al., 2016).

Pre-processing of the fMRI dataset included a first step to verify the absence of any outlier (i.e. corrupted volume by spikes, etc.). Standard preprocessing was performed using Nipype (Gorgolewski et al., 2011), including slice timing and motion correction, as in previous studies using the ARCHI dataset (Bzdok et al., 2016). The T1-weighted scan was used as a reference and both fMRI and fieldmap datasets were matched to this reference using a mutual-information based registration algorithm providing the corresponding rigid transformations T(fMRI→T1) and T(B0→T1). Unwrapping of the phase difference map included in the fieldmap scan was performed using a weighted full multigrid phase unwrapper algorithm that did not require the preliminary definition of a mask of the brain, and the unwrapped phase map was then matched to the fMRI dataset by composition of the former transformations in order to correct for susceptibility artifacts. Finally, bandpass filtering with $[0.01\ -0.1]$ Hz was applied to the signal resulting from the averaging over each ROI.

Table 1
List of the 34 ROI labels for the Desikan parcellation (Desikan et al., 2006). The order of Fig. 4a, from bottom to top. The parcellation has 1 such ROI for each hemisphere.

Label	Description
CUN	cuneus
PCAL	pericalcarine gyrus
LING	lingual gyrus
LOCC	lateral occipital cortex
FUS	fusiform gyrus
BSTS	bank of superior temporal sulcus
IT	inferior temporal cortex
MT	middle temporal cortex
ST	superior temporal cortex
TT	transverse temporal cortex
TP	temporal pole
PCUN	precuneus
SMAR	supramarginal cortex
IP	inferior parietal cortex
SP	superior parietal gyrus
PARC	paracentral gyrus
PREC	precentral gyrus
PSTC	postcentral gyrus
ENT	entorhinal gyrus
PARH	parahippocampal cortex
INS	insula
CAC	caudal anterior cingulate cortex
RAC	rostral anterior cingulate cortex
PC	posterior cingulate cortex
ISTC	isthmus of cingulate cortex
SF	superior frontal cortex
CMF	caudal middle frontal cortex
RMF	rostral middle frontal cortex
POPE	pars opercularis
PORB	pars orbitalis
PTRI	pars triangularis
LOF	lateral orbitrofrontal medial cortex
MOF	medial orbitrofrontal medial cortex
FP	frontal pole

2.2. MOU process fitted on whole-brain fMRI data

We now review important properties of the dynamic model that has been developed in previous work (Gilson et al., 2016). A motivation for using the MOU process is because its Green function has an analytical formulation, related to the matrix exponential (Gilson et al., 2018). The MOU process is determined by (i) a local leakage related to the decay time constant τ, (ii) a directed weighted matrix A associated with linear coupling that is the MOU-EC and (iii) fluctuating inputs with zero mean and a given covariance matrix Σ. Assuming stationarity over each resting-state session, we estimate τ, A and Σ using a form of gradient descent performed without simulating the network activity, but using analytical consistency equations. This optimization procedure has a single solution in the absence of observation noise (Gilson et al., 2016).

The following mathematical details will be useful for the calculation of our graph-like measures. Formally, the MOU process in matrix form is defined as

$$\mathrm{d}\mathbf{x}^t = J\mathbf{x}^t\,\mathrm{d}t\ +\ \mathrm{d}\boldsymbol{\zeta}^t\ , \tag{1}$$

where the Jacobian matrix J is determined by the decay time constant τ (identical for all ROIs) and A_{ij} is the MOU-EC weight from ROI j to ROI i (different from the usual convention in graph theory):

$$J_{ij} = -\frac{\delta_{ij}}{\tau} + A_{ij}\ ; \tag{2}$$

here δ_{ij} is the Kronecker delta (equal to 1 when $i = j$ and 0 otherwise). Similar to a transition matrix for a Markov chain, the matrix A determines the Jacobian of the dynamic system. The time constant τ is an abstraction of the hemodynamic response decay. The choice of a single time constant τ for all ROIs, but individual for each subject, comes from the data, which exhibit a smaller variability across ROIs than across subjects (not shown here). Last, the fluctuating input to ROI i is denoted by ζ_i and represents spontaneous activity. Formally, ζ is a Wiener process (or temporally white noise) with covariance matrix

$$\Sigma = \langle \mathrm{d}\boldsymbol{\zeta}^t (\mathrm{d}\boldsymbol{\zeta}^t)^\dagger \rangle\ , \tag{3}$$

where the angular brackets $\langle\cdots\rangle$ indicate the statistical average and $\dagger$ the matrix transpose. In the present study the matrix Σ is kept diagonal, meaning that ζ_i are independent white noise. However, it may also involve cross-covariances (Gilson et al., 2018b). To ensure stable dynamics, the Jacobian J must have eigenvalues with strictly negative real part. In particular, the dominating eigenvalue (or spectral diameter) of the weight matrix A needs to satisfy $\lambda_{\max} < -1/\tau$, meaning that the local leakage must be sufficiently quick (or strong) compared to the global network feedback.

The MOU-EC weights A_{ij} come from the tuning of the model to reproduce the spatio-temporal structure of the BOLD signals, which is simply the pair of covariance matrices FC0 and FC1 in Fig. 1a. For the model activity, these covariance matrices are defined as

$$Q^\tau = \langle x^t (x^{t+\tau})^\dagger \rangle\ , \tag{4}$$

without time lag for $\tau = 0$ and with a time lag $\tau = 1$ TR (temporal resolution of the BOLD measurements). The Lyapunov optimization (akin to a gradient descent) iteratively adjusts the weights A_{ij} for each existing connection, the variance Σ_{ii} for each ROI and a common τ for all ROIs to reproduce the covariances of fMRI signals involving time shifts

Table 2
This table shows which properties of the original network are preserved (√) or randomized (×) by the surrogates.

Property	random	null	ring	short ring
Mean weight	√	√	√	√
In weight for each ROI	×	√	√	√
Out weight for each ROI	×	√	×	×
Density	√	×	√	×

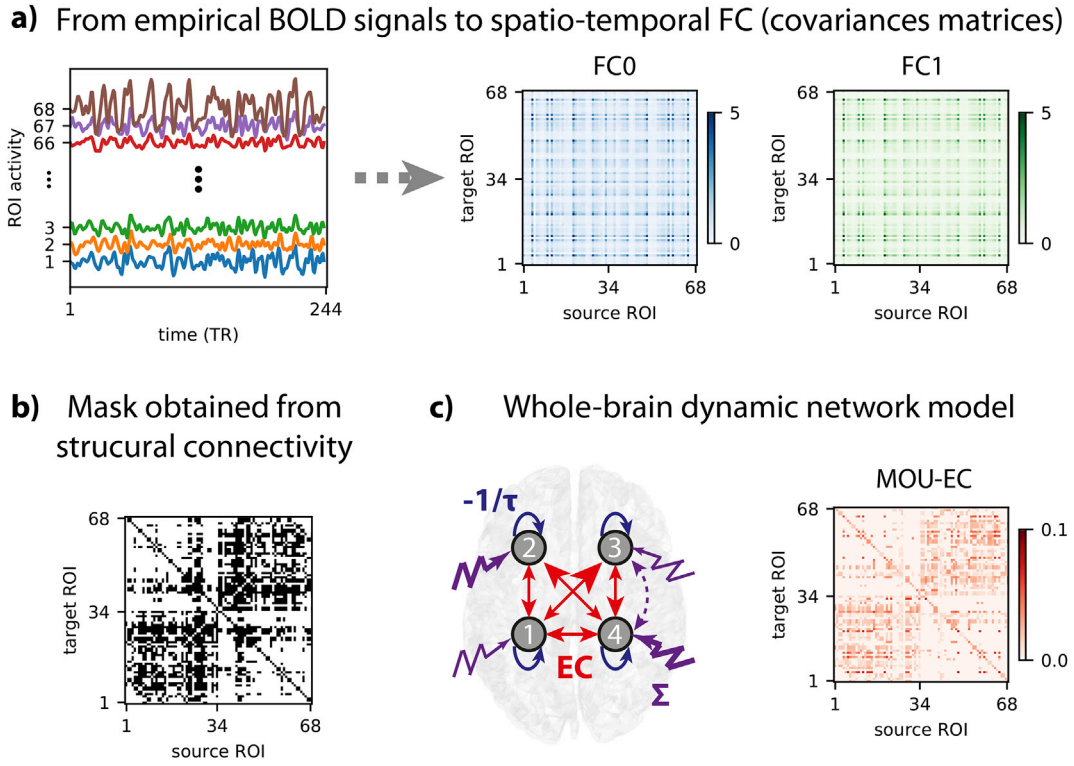

Fig. 1. MOU-EC estimation. a) From the fMRI signals (left plot), the covariance matrices FC0 and FC1 are calculated, represented in blue and green respectively. FC0 is the zero-lag covariance and FC1 corresponds to a time shift of 1 TR. **b)** Topological mask for existing connections in the model obtained from thresholding the average SC over subjects. **c)** The network parameters comprise of the MOU-EC matrix A (red arrows in the left diagram) and self-inhibition corresponding to the time constant τ (blue arrows), see Eq. (2). Note that A is not a full matrix, because its topology is determined by the mask obtained from SC in panel b. In addition, the local excitabilities or inputs (purple arrows) are determined by their covariance matrix Σ. Here only 4 ROIs are represented for readability. In this paper the focus on the estimated MOU-EC matrix, corresponding to matrix A in Methods, as well as the leakage time constant τ involved in Eq.(2). For each session, A is estimated from the covariance matrices FC0 and FC1, capturing the average BOLD transition statistics over the session (assuming stationarity). Further details about the dynamic model and estimation procedure can be found in previous studies (Gilson et al., 2016, 2018b).

(empirical FC matrices). The optimization steps are repeated until reaching a minimum in the model error, which is the matrix distance between corresponding model and empirical FC0/FC1. Details can be found in previous papers (Gilson et al., 2016, 2018b). Note that we use simplified notation for compactness here, as compared to those previous publications.

The estimated MOU-EC is in general a directed and weighted matrix (Gilson et al., 2016). EC is also "sparse" with density 34%, corresponding to 1562 non-zero elements among the $N(N-1) = 4556$ off-diagonal matrix elements. To determine the MOU-EC topology (which connections between ROIs exist in the model), we average the SC matrices over all subjects and threshold to keep the strongest anatomical links. This reduces the number of parameters (including 68 for Σ) and improves the robustness of the estimation as each session has $244 \times 68 = 16592$ time points over all ROIs. Importantly, the individual values of the estimated MOU-EC weights do not depend on SC values, but are determined by the optimization procedure for the model FC that best reproduces the empirical FC.

The model optimization approach contrasts to previous studies that used SC values for the connectivity weights in their model, while tuning local dynamics such as Kuramoto oscillators or mean-field approximation of spiking neurons (Cabral et al., 2011; Deco et al., 2013; Messé et al., 2014). Our estimation procedure can be seen as a "projection" of the empirical spatio-temporal BOLD structure on the space of model parameters, where MOU-EC captures the propagating nature of the BOLD signals.

We use the EC terminology that originates from electrophysiology and was further developed in the literature of the DCM. In our case MOU-EC is the underlying connectivity in a generative dynamic model of BOLD activity, which corresponds to a historical key aspect of the EC concept. However, our model does not involve the hemodynamic response and differs from state-space models such as the DCM that separates the neuronal network and the generation of BOLD activity (Friston, 2011; Valdes-Sosa et al., 2011). The differences between MOU-EC estimation and other related methods will be reviewed of the Discussion.

2.3. *Dynamic communicability measures interactions between ROIs across time*

Following our previous paper (Gilson et al., 2018), we define *dynamic communicability* to characterize the network interactions induced by its weighted and directed connectivity A, ignoring the input properties Σ.

This definition is adapted to study complex networks associated with realistic (stable) dynamics where time has a natural and concrete meaning, with the Jacobian J combining A and the leakage time constant τ. In comparison, a previous version of communicability for graphs (Estrada and Hatano, 2008) relies on abstract dynamics. From the graph communicability e^A based on the matrix exponential, the strengths $\sum_i (e^A)_{ij}$ and $\sum_j (e^A)_{ij}$ were used to evaluate the roles for nodes as broadcasters or listeners in the network (Estrada, 2013). The diagonal elements $(e^A)_{ii}$ quantify the feedback received by a node from its own abstract "activity" and was used to define centrality (Benzi and Klymko, 2013). Getting inspiration from those studies, we base our framework of dynamic communicability on the Green function (or network impulse response) to perturbation for the MOU process, focusing on the temporal evolution of such interactions (see dashed arrow in Fig. 2a). The present study uses the MOU process because of its analytical tractability, but our framework can be applied to any local dynamics for which the Green function is known.

Dynamic communicability measures the network response when applying a perturbation to a given node (node 1 in Fig. 2a). Importantly, communicability excludes the "intrinsic" relaxing response due to the local leakage to focus on the contribution of the connectivity A to the network response, see the zero communicability for node 1. Note that the strong weight A_{23} from node 2 to node 3 gives to a strong communicability between 1 and 3, even though A_{21} is small. For recurrent networks, the existence of feedback loops gives a positive communicability for a node onto itself; see the green and blue curves in the top and middle configurations in Fig. 2b. For the MOU process, communicability is the "deformation" of its Green function e^{Jt} due to the presence of the matrix A (dashed curves), as compared to the Green function $e^{J^0 t}$ corresponding to the Jacobian with leakage only and no connectivity, $J^0_{ij} = -\delta_{ij}/\tau$ (dotted curves). It is embodied by the family of time-dependent matrices (see also Fig. 3a in Results):

$$\mathscr{C}(t) = \left|\left|J^0\right|\right| \left(e^{Jt} - e^{J^0 t}\right) . \tag{5}$$

From now on, recall that $t \geq 0$ is the time for the propagation of activity in the network, referred to as 'integration time', which is different from the time from Eq. (1) to Eq. (4). The scaling factor $||J^0||^{-1} = \left|\left|\int_{t\geq 0} e^{J^0 t} dt\right|\right|$ where $||\cdot||$ is the L1-norm for matrices (i.e. sum of elements in absolute value) is used for normalization purpose, e.g. when comparing networks of distinct sizes (Gilson et al., 2018).

From each matrix $\mathscr{C}(t)$, we define the total communicability as the sum of all interactions

$$\mathscr{S}^{\mathscr{C}}(t) = \sum_{\{i,j\}} \mathscr{C}_{ij}(t) . \tag{6}$$

Total communicability measures the effect, after the integration time t, of a simultaneous perturbation applied to all nodes at time $t = 0$. The function $\mathscr{S}^{\mathscr{C}}(t)$ reflects the global network feedback determined by the matrix A and more precisely relates to eigencentrality as it is mainly determined by the largest eigenvalue of A (Gilson et al., 2018). We also define the diversity (or heterogeneity) among the ROI interactions in the time-dependent matrices $\mathscr{C}(t)$, which can be seen as a proxy for their homogenization over time:

$$\mathscr{D}^{\mathscr{C}}(t) = \frac{\sigma_{\{i,j\}}\left[\mathscr{C}_{ij}(t)\right]}{\mu_{\{i,j\}}\left[\mathscr{C}_{ij}(t)\right]} , \tag{7}$$

defined as a coefficient of variation where $\mu_{\{i,j\}}$ and $\sigma_{\{i,j\}}$ are the mean and standard deviation over the matrix elements indexed by (i,j). In Fig. 2b the top configuration has the same communicability from node 1 to node 2 (in purple) as from 2 to 1 (in cyan), because the corresponding weights in A are identical. For the unbalanced connectivity in the bottom configuration, the communicability from 1 to 2 is larger than the converse. Because both network configurations have the same sums $A_{12} + A_{21}$, they have very similar total communicability $\mathscr{S}^{\mathscr{C}}(t)$ in Fig. 2c, but distinct diversity $\mathscr{D}^{\mathscr{C}}(t)$.

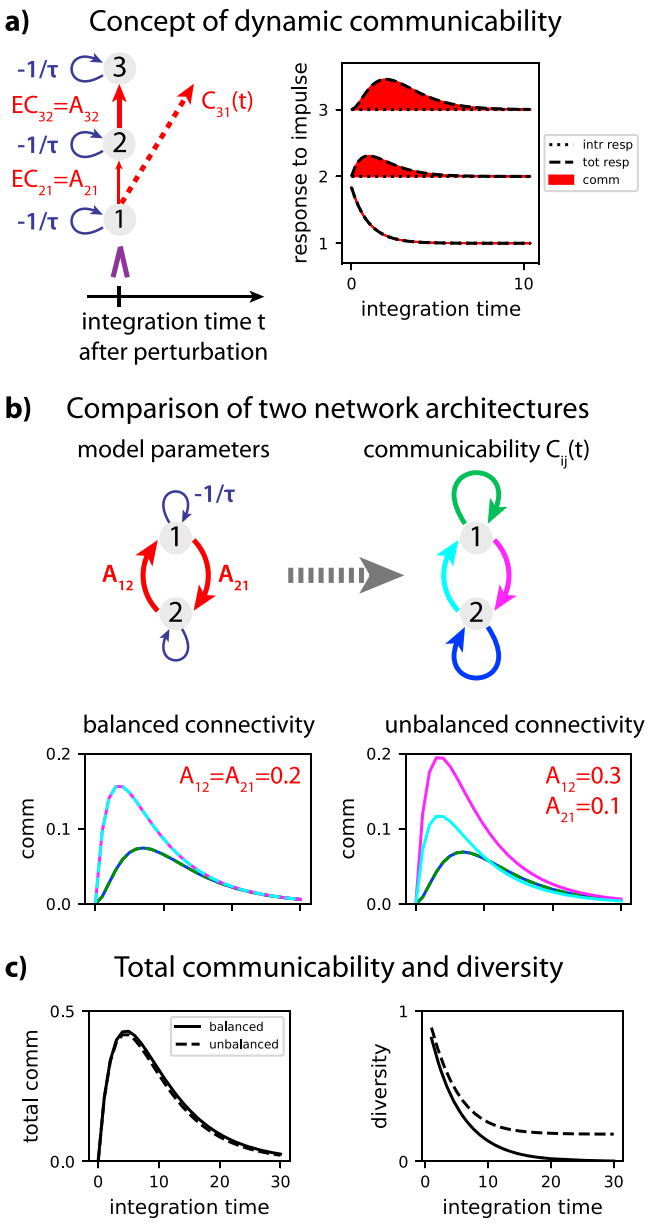

Fig. 2. Concept of dynamic communicability. a) Communicability for three nodes relies on the response of the network to a unit perturbation at a given node (here node 1). The dynamics are determined by local leakage related to the time constant τ and the connectivity weights A (left diagram). In the right plot the total response of the is represented in dashed line and the "intrinsic" response due to leakage only in dotted line, corresponding to J^0 in Eq. (5). The communicability $\mathscr{C}(t)$ is the difference between these two curves. **b)** The left diagram represents a network of two nodes with recurrent connections. Its communicability $\mathscr{C}(t)$ is a 2×2 matrix with 4 elements (see green, blue, purple and cyan arrows in the right diagram). The bottom plots compare the communicability for the two network configurations. Note that the blue and green curves are superposed. **c)** Total communicability $\mathscr{S}^{\mathscr{C}}(t)$ in Eq. (6) and diversity $\mathscr{D}^{\mathscr{C}}(t)$ in Eq. (7) for both networks. The solid curves correspond to the balance network and the dashed curves to the unbalanced one.

2.4. Community detection

To detect communities based on communicability, we rely on New-

man's greedy algorithm for modularity (Newman, 2006) that was originally designed for weight-based communities in a graph. Adapting it here to the matrix $\mathscr{C}(t)$ at a given time t, we seek for communities where ROIs have strong bidirectional interactions. In the same manner as with weighted modularity, we calculate a null model for EC:

$$A^{\text{null}} = \frac{\mathbf{a}^{\text{in}}\mathbf{a}^{\text{out}\dagger}}{\mathscr{S}^A} \,. \tag{8}$$

Note that we preserve the empty diagonal ($A^{\text{null}}_{ii} = 0$). The resulting matrix contains from the expected weight for each connection, given the observed input strengths $\mathbf{a}^{\text{in}}$ and output strengths $\mathbf{a}^{\text{out}}$; $\mathscr{S}^A$ is the total sum of the weights in A. Then we calculate $\mathscr{C}^{\text{null}}(t)$ using Eq. (5) with A^{null} instead of A. Starting from a partition where each ROI is a singleton community, the algorithm iteratively aggregates ROIs to form a partition of K communities denoted by S_k that maximizes the following quality function:

$$\Phi = \sum_{1\le k\le K} \sum_{i,j\in S_k} \left(\mathscr{C}(t) - \mathscr{C}^{\text{null}}(t)\right)_{ij} + \left(\mathscr{C}(t) - \mathscr{C}^{\text{null}}(t)\right)_{ji} \,. \tag{9}$$

At each step of the greedy algorithm, the merging of two of the current communities that maximizes the increase of Φ is performed.

3. Results

This section uses our definitions of dynamic communicability to interpret resting-state fMRI data (see Fig. 3a). The data were recorded from 77 subjects during 244 frames each separated by a TR = 2.4 s with eyes closed in a scanner. Our framework relies on a dynamic system and, for illustration purpose, the present study uses our recent optimization to fit the MOU model to BOLD signals (Gilson et al., 2016, 2018b); the python code is available on github.com/MatthieuGilson/WBLEC_toolbox).

After recapitulating some key properties of the MOU-EC model, we use dynamic communicability to characterize the network properties at various scales, from the whole network to individual ROIs. In particular, we compare dynamic communicability with FC to stress the importance of incorporating time in the analysis. We then study the complexity of the estimated MOU-EC network by contrasting it with reference networks like ring lattices used in the context of small-worldness. To further examine the network organization, we finally detect communities based on dynamic communicability, which provide a collective description at an intermediate level between ROIs and the whole network.

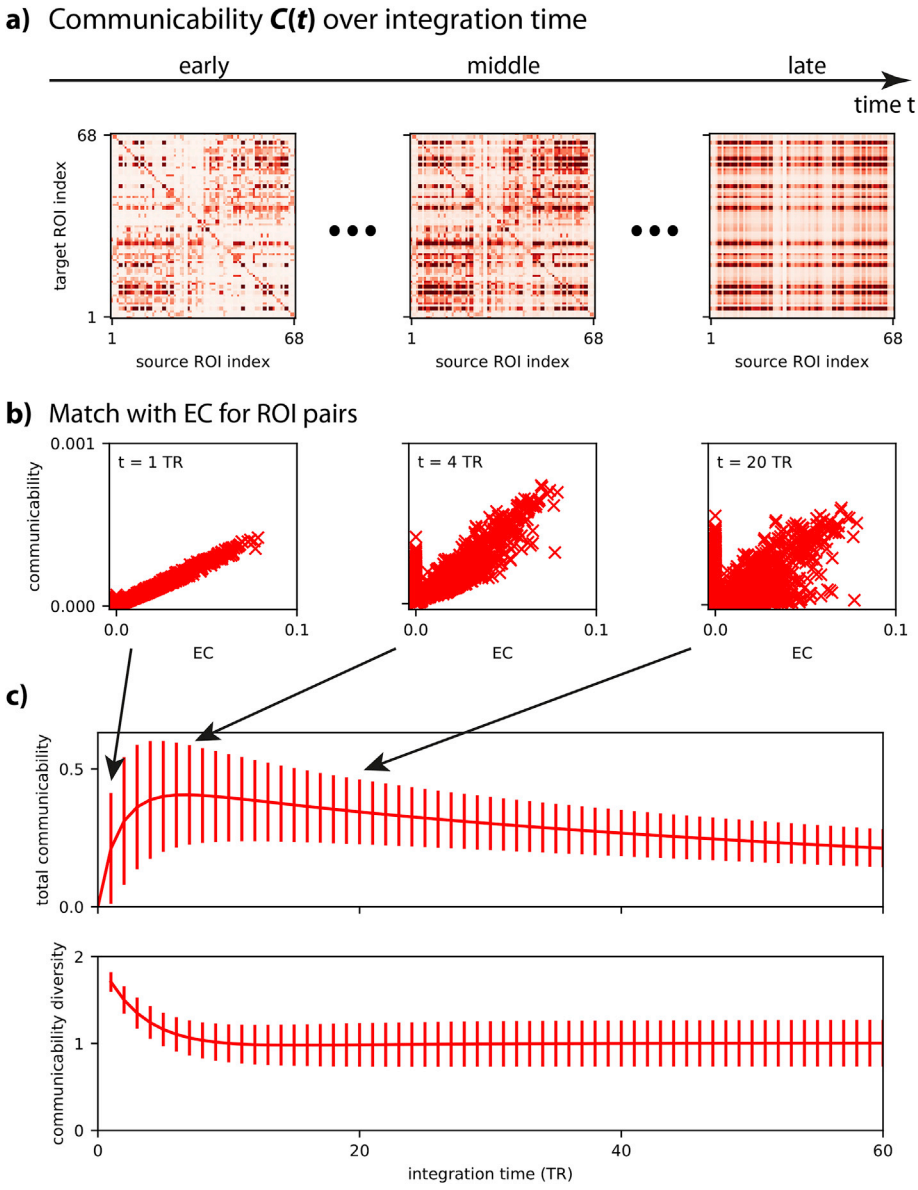

Figure 3. Whole-brain dynamic communicability. **a)** Communicability for a single subject, corresponding to the family of matrices $\mathscr{C}(t)$ in Eq. (5) that involves the matrix exponential of the Jacobian multiplied by time $t \geq 0$. Recall that t corresponds to the integration time after perturbation in the network. The range is the same as the MOU-EC matrix in panel a. **b)** Match between MOU-EC and communicability for each pair of ROIs (red crosses) at three times for the same subject as in panel b. **c)** Total communicability $\mathscr{T}^{\mathscr{C}}$ defined as in Eq. (6) reflects the global network feedback. The x-axis represents the integration time in units of the scanner measurements (time resolution, or TR, equal to 2.4 s). The curves correspond to the average over the 77 subjects and the error bars the standard deviation. Diversity of communicability $\mathscr{D}^{\mathscr{C}}$ defined as in Eq. (7) that quantifies the homogenization of interactions across time.

3.1. MOU-EC estimation captures the BOLD dynamics

This model optimization combines several key aspects that are developed in Methods:

- A whole-brain approach (Deco et al., 2011) is necessary to properly take into account the distributed nature of information conveyed by BOLD signals, as was experimentally observed for high-level cognition (Chang et al., 2015) or neuropathologies (Deco and Kringelbach, 2014).
- The MOU process is optimized to reproduce the spatio-temporal structure of the BOLD signals, which was shown to convey information about the behavioral condition of subjects (He, 2011; Ciuciu et al., 2014; Mitra et al., 2015). This contrasts to traditional analyses of the "spatial" FC, which does not involve time lags.
- The optimization combines information from both FC and SC data in estimating the MOU-EC (Gilson et al., 2016), which is then subject/condition-dependent with a "sparse" topology corresponding to the anatomy.
- In the model the directional connections between brain regions describe causal interactions between ROIs. However, recall that the hemodynamic response is not explicitly modeled in our MOU process. Therefore, the interpretation of the DCM-EC, estimated with an explicit modeling of the hemodynamics (Friston, 2011; Valdes-Sosa et al., 2011), is closer to neuronal connectivity compared to our MOU-EC.

The use of whole-brain directional connectivity is the feature that makes the application of dynamic communicability interesting. Another motivation for using MOU-EC is that the leakage time constant τ, which is part of the Jacobian J in Eq. (2), is estimated during the model optimization. In contrast, taking SC or another directed connectivity matrix (e.g. obtained using Granger causality) as matrix A in J to use Eq. (5) would require an arbitrary choice for τ, because they are not estimated with the dynamic model. Note also that the heterogeneity of the Σ estimates (see purple arrows with various thicknesses in Fig. 1c) is ignored in the present analysis and left for future work.

3.2. Dynamic communicability provides both global and local information about the brain network

In the present formalism, communicability is the family of matrices $\mathscr{C}(t)$ in Fig. 3a that describe the interactions between pairs of ROIs across time. In each matrix $\mathscr{C}(t)$, a column measures how a unit perturbation applied at $t = 0$ to the corresponding source ROI propagates throughout the network via the recurrent MOU-EC and impacts the other target ROIs after a delay t —termed 'integration time'— during which the network effect builds up. The theory is based on the Green function or impulse response of the network, see Eq. (5) in Methods. This directed measure thus integrates all possible pathways between the source and target ROIs, while taking the nodal dynamics of the model into account (here a exponential decay related to a time constant τ, see Fig. 1c). For the resting-state, perturbations are the fluctuations at each ROI, whose effects sums over time.

Initially aligned with MOU-EC (i.e. interactions through the strong direct connections dominate), the pattern of communicability progressively reshapes and the influence of connections with strong weights dilutes, as illustrated in Fig. 3b. In particular, unconnected regions may have strong communicability due to network effects (see crosses for $A_{ij} = 0$ on the left of the plots). This homogenization results from the superposed loops in the MOU-EC matrix that generate a strong overall feedback that distributes the effect of the fluctuations.

The strong network feedback is reflected in the total dynamic communicability $\mathscr{S}^{\mathscr{C}}$ in the top panel of Fig. 3c, which rises to reach a maximum around 7 TR, before decaying very slowly. The integration time of the peak corresponds to the lag after which a perturbation in the network (here affecting all nodes) has the maximum influence (given by the size of the peak), due to the building up of the network effect. The slow decay afterwards indicates that the effect persists over time. The homogenization is reflected in the communicability diversity $\mathscr{D}^{\mathscr{C}}$ (bottom panel) that quickly decays to stabilize after 15 TR. This defines the temporal horizon after which the effect of perturbations are most broadly distributed across the network. Note that, meanwhile, $\mathscr{S}^{\mathscr{C}}$ is still high. These curves provide a signature for the estimated MOU-EC, which can be analyzed to uncover its topological properties.

3.3. ROI-specific analysis and comparison with SC and FC

The brain network structure determines a hierarchy among ROIs. For binary graphs, the notions of degree and centrality have been used to detect highly connected ROIs, or hubs that have strong influence on other nodes. This type of approach has been used to explore the importance of ROIs in the brain based on SC or FC data (Zamora-López et al., 2009; van den Heuvel et al., 2012; Sporns, 2013). A limitation is that SC and FC do not have directional information (i.e. they are symmetric matrices). Graph communicability (Estrada, 2013) can be used to describe differentiated input and output properties for the ROIs. We now show how our dynamic communicability can be used to characterize ROIs in the network and incorporating the temporal dimension.

The overall picture obtained from MOU-EC is differentiated roles across ROIs, each with its own amplitude (in red in Fig. 4a) and timescale (Fig. 4b). In general, ROIs have distinct input and output communicability (Fig. 4c), thus defining listeners and broadcasters. This relates to the propagating nature of fMRI signals, which is related to the asymmetry of estimated MOU-EC matrices (Gilson et al., 2016) and is in line with previous results of the fMRI lag structure (Mitra et al., 2015). Compared to our previous analyses that focused on individual MOU-EC connections (Gilson et al., 2018b; Senden et al., 2018), communicability provides a description of the ROI role over time. ROIs usually classified as hubs according to their high degree in SC (in black in Fig. 4a) are indicated by the black crosses: the precuneus (PCUN), superior frontal cortex (SF) and superior parietal cortex (SP). PCUN and SP exhibit strong input communicability, which classifies them as listening ROIs, integrating the activity from the rest of the brain. This is in line with previous results that suggested a global integration role for PCUN as part of the default mode network (Vatansever et al., 2015). In comparison, SF has more balanced (and weaker) input and output communicabilities. The visual ROIs (CUN, PCAL, LING and LOCC) are both listeners and broadcasters. Other noteworthy ROIs with strong output communicability are the pre- and postcentral ROIs (PREC and PSTC), as well as the superior temporal ROIs (ST).

At the global level, previous work (Raemaekers et al., 2018) showed asymmetries in the left and right within-hemisphere FC patterns. In contrasts, we observe for our data a symmetric communicability for the two hemispheres in Fig. 4d. Moreover, the communicability is initially higher within each hemisphere (solid curves) than between hemispheres (dashed curves), but rapidly reaches similar values around 20 TR. This points to slightly weaker inter-hemispheric communication compared to within-hemispheric communication at rest. It can be explained by the difference in connectivity degree of the between/within hemispheric MOU-EC weights, as similar curves can be obtained using the binarized MOU-EC estimate with ad-hoc rescaling (giving the matrix in Fig. 1b). Our previous results based on MOU-EC indicated stronger inter-hemispheric communication when analyzing changes of individual MOU-EC weights when engaging a passive-visual task (Gilson et al., 2018b), which would be interesting to quantify at the network level using the present formalism.

Comparing FC strengths and SC degrees with communicability in Fig. 4a, we observe that the correspondence between strong values is not trivial. To further quantify this relationship, we display these ROI-specific measures as scatter plots in Fig. 5a–b, where communicability

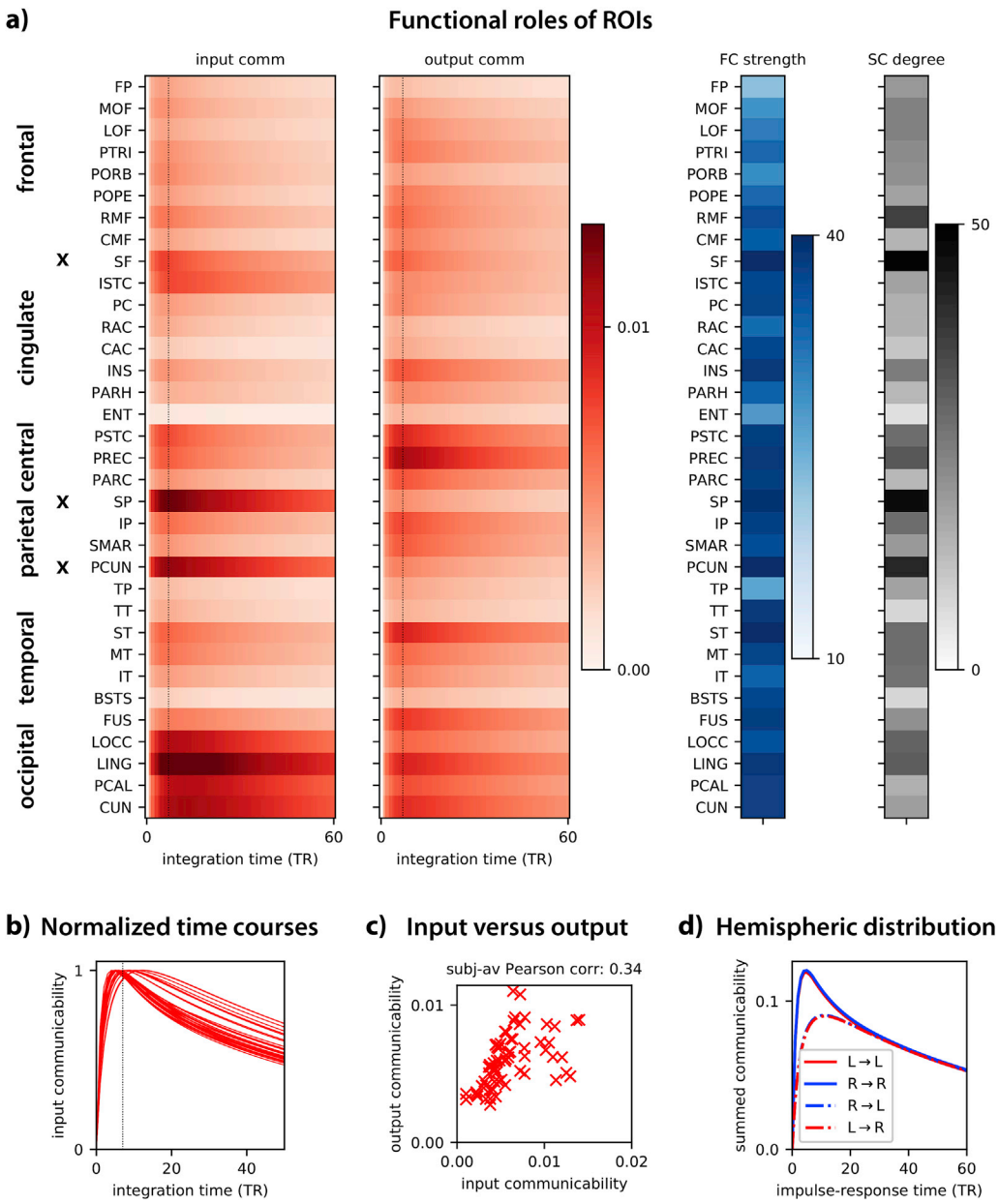

Fig. 4. Characterization of ROI roles. **a)** Temporal evolution of input and output communicability for all ROIs (in red). The values are averages over the two hemispheres and all subjects. The ROIs are grouped by anatomical areas and black crosses indicate the three pairs of rich-club ROIs. The dotted vertical lines indicate the maximum for the average $\mathscr{S}^{\mathscr{C}}$ over subjects in Fig. 3c, corresponding to $t = 7$ TR. The right plots indicates the FC strengths (in blue) and SC degrees (in black). Here recall that FC is the classical Pearson correlation between the BOLD signals (not covariances as in Fig. 1). **b)** The normalized time courses for input communicability reveal a variety of timescales across the ROIs. **c)** Comparison of input and output communicability for each ROI (red cross). The plotted values are taken at $t = 7$ TR indicated by the dashed vertical lines in panel a. **d)** Evolution of the total communicability within and between the two hemispheres (L for left and R for right).

is taken at the peak at $t = 7$ TR (dotted line in Fig. 5a–b). We find that input communicability correlates with the SC degree (dark red dots), as measured by a Pearson correlation of 0.58 (evaluated for each subject, then averaged over them). This suggests that regions with strong input communicability have sufficiently many connections to support it. Moreover, output communicability correlates with FC strengths (purple triangles) with a Pearson correlation of 0.51. It is smaller than 0.35 otherwise, in the same range obtained for the relationship between SC and FC in Fig. 5c. Even though the general relationship is positive correlations between these descriptors, our model-based approach provides distinct information from the classical analyses based on SC/FC alone. When varying the integration time for input/output communicability, we see that the Pearson correlation is stable in Fig. 5d, except for a transient peak for input communicability and SC degree. This can be explained because of the equal sparsity between these two matrices for early integration times.

Previous studies showed how MOU-EC weights are modulated in a task-dependent manner (Gilson et al., 2018b; Senden et al., 2018). In particular, the output MOU-EC weights of hubs are down-regulated at rest as compared to visual tasks (Senden et al., 2018). This suggests that not all existing MOU-EC pathways are used at rest, which may explain the very weak correlation of output communicability with SC in Fig. 5.

3.4. Comparison with reference networks

Communicability enables the quantitative comparison of the estimate for brain dynamics with other reference network models. Here we compare the global measures of total communicability $\mathscr{S}^{\mathscr{C}}$ and its diversity $\mathscr{D}^{\mathscr{C}}$ in Fig. 3d to their counterparts for surrogate networks obtained by manipulating the MOU-EC estimates. The comparison between the timescales associated with the corresponding curves provides insight about equivalent topologies to generate dynamics similar to the model estimates. Topological properties such as strong feedback and short path length are reflected in $\mathscr{S}^{\mathscr{C}}$ and $\mathscr{D}^{\mathscr{C}}$ (Gilson et al., 2018).

In Fig. 6d, the evolution of $\mathscr{S}^{\mathscr{C}}$ and $\mathscr{D}^{\mathscr{C}}$ for the original data (red curves) is compared with four surrogate models:

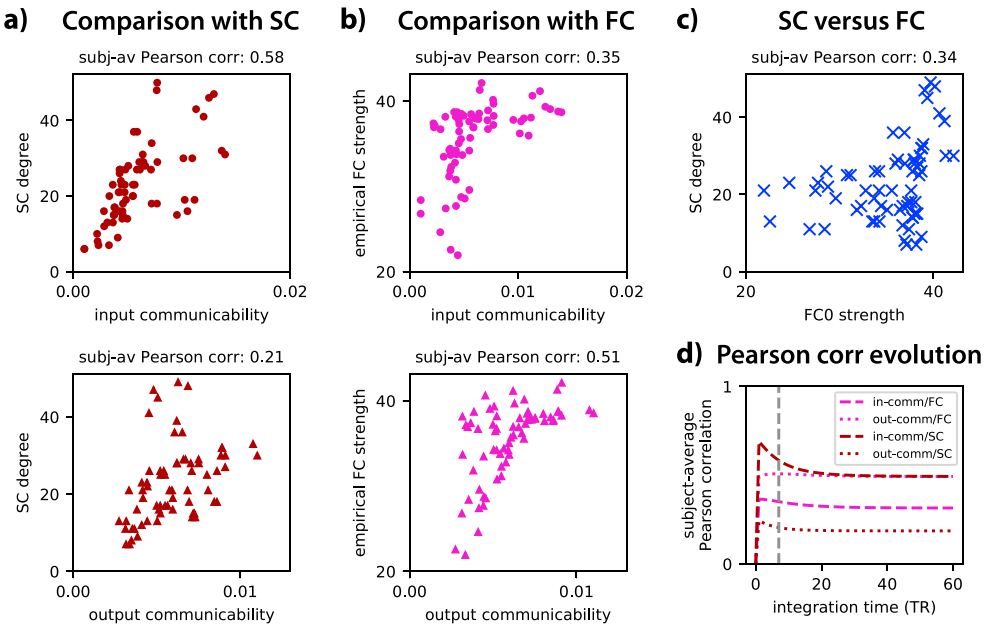

Fig. 5. Comparison with SC and FC. a) Comparison of the input and output communicability (left and right panels in each row with dots and triangles, resp.) with the SC degree. Each symbol represents the value for an ROI, averaged over all subjects; for communicability, it is taken at integration time 7 TR corresponding to the dashed vertical lines in Fig. 4a. The Pearson correlation coefficient above each plot corresponds to the average over all subjects. **b)** Same as panel a for empirical FC strengths. **c)** Comparison between SC degrees and strengths with empirical FC strengths. The value above the plot is the average over subjects of the Pearson correlation between individual input and output communicability. **d)** Evolution of the Pearson statistics when varying the integration time (x-axis).

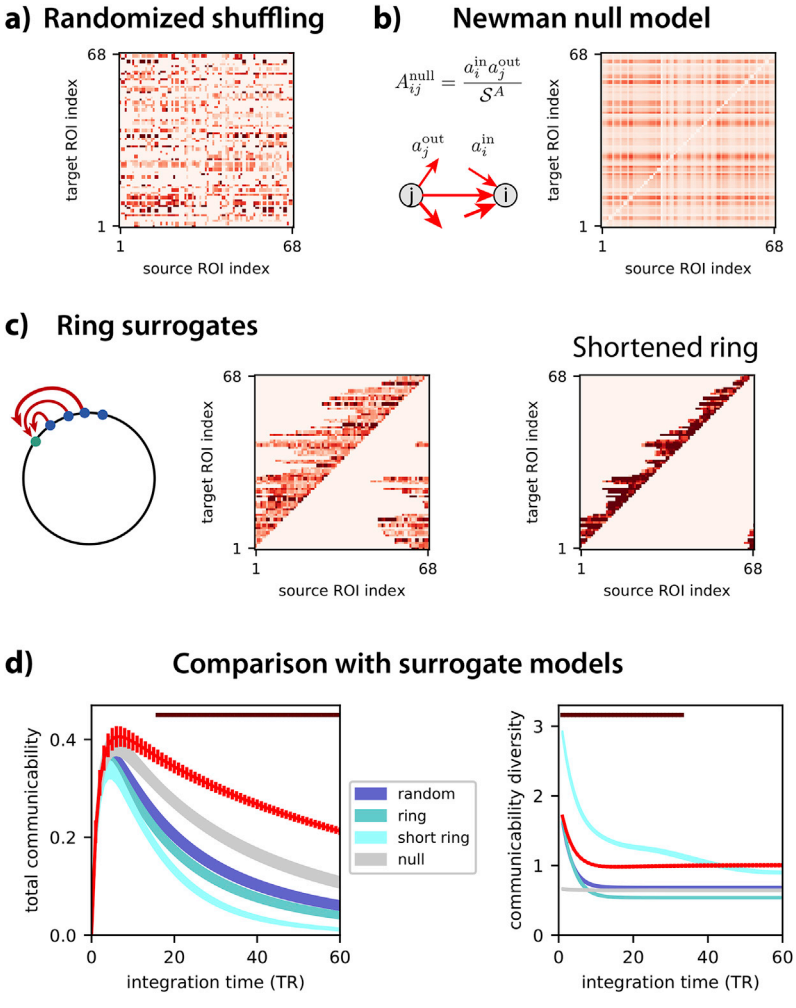

Fig. 6. Comparison of the estimated model with surrogates. a) Randomized version of the estimated matrix A by globally shuffling the target ROIs. The range of the matrix weights (as well as other panels in this figure) is the same as in Fig. 3b **b)** The null-model connectivity is calculated using Eq. (8) redistributes the weights while preserving the input and output strengths for each ROI. This results in a full matrix, apart from the empty diagonal. **c)** The ring surrogates consider the initial ROI order and reallocate the non-zero weights in the original A to the preceding ROIs. The ring preserves the number of connections (hence the density), whereas the shortened ring corresponds to grouping connections three by three, resulting in fewer connections. **d)** The total communicability $\mathscr{TC}$ and the corresponding diversity $\mathscr{DC}$ in red are the same as in Fig. 3d, but the error bars indicate the standard error of the mean here (much smaller than the standard deviation). The colored areas correspond to the surrogate networks in panels a to c, which preserve part of the connectivity statistics of the original A (see Table 2). The transformations are applied individually for each subject. The variability of the curves (represented by the thickness of the plotted area) corresponds to the standard error of the means over subjects, as error bars for the red curve. The dark red bars over the curves indicate the integration times where the model is significantly different from all surrogates, as measured by the Mann-Whitney test for which the p-value is smaller than 0.001 for all 4 comparisons (uncorrected).

- The random surrogate in Fig. 6a reallocates the weights to a pair of ROIs. The exact weight distribution is conserved in the network, but not for each ROIs.
- The null model in Fig. 6b was proposed for Newman modularity (Newman, 2006) to detect communities and corresponds to resulting a full matrix with for each pair of ROIs the expected weight that

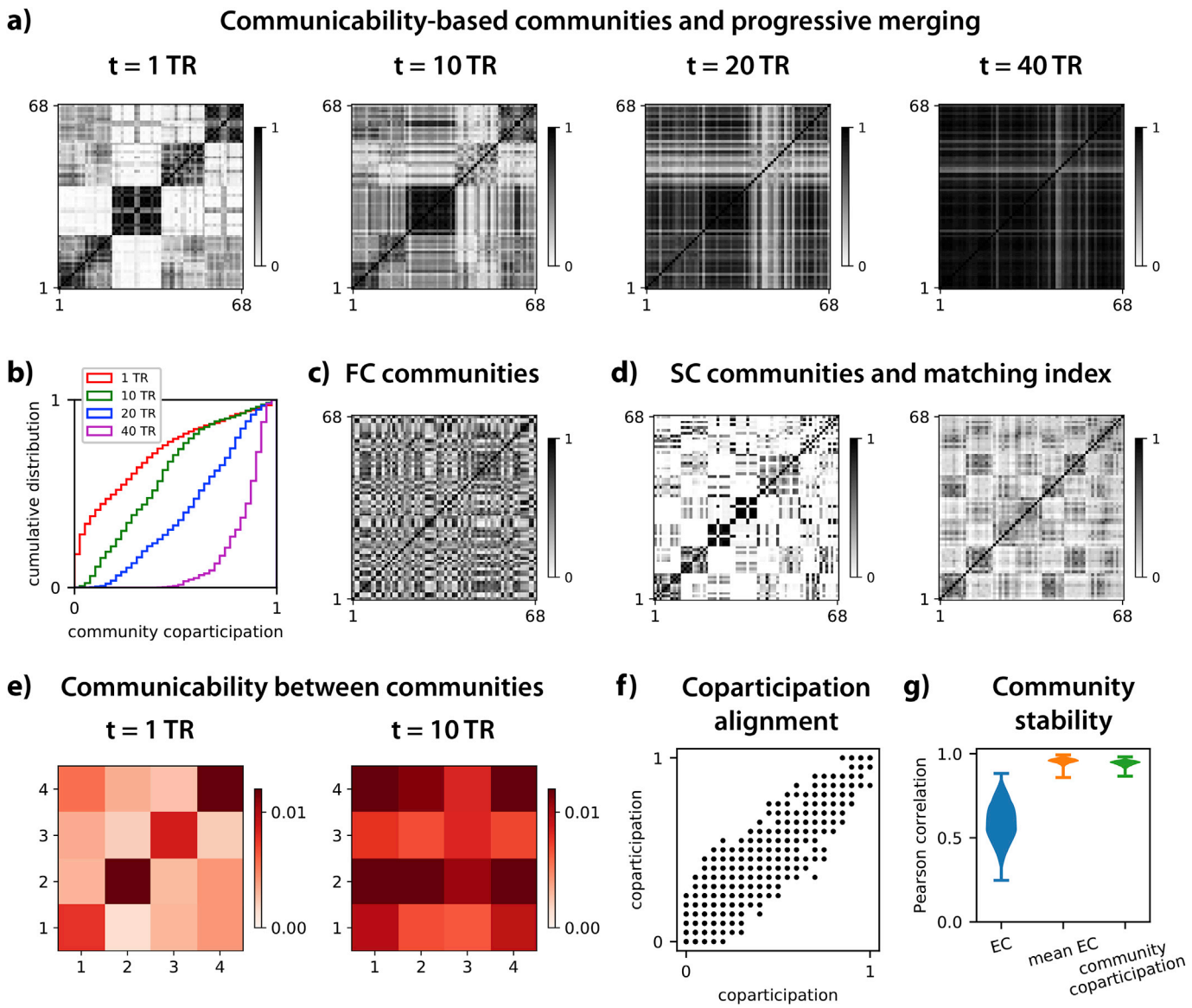

Fig. 7. Communicability-based communities and homogenization of cortical activity. a) Each matrix represents the communities of cortical regions with strong communicability for four values of integration time *t*. Regions are paired when they have strong bidirectional communicability between them, see Eq. (9) for details. They correspond to averages over the 77 subjects and darker pixels indicate that the two regions (on the x- and y-axis) belong to the same community over all subjects. The region ordering is the same for all plots and is chosen to highlight the 4 communities (dark blocks on the diagonal). The x-axis indicate source ROIs and the y-axis target ROIs. **b)** Cumulative distribution of the community coparticipation values in panel a for the 4 matrices in panel a, illustrating the merging of communities. **c)** Similar plots to panel a with the FC-based communities. **d)** Similar plot (left panel) to panel a for SC-based communities obtained with the individual matrix with DWI values, see Methods. The right panel display the matrix of matching indices for SC, which measures the overlap between connected targets for each pair of ROIs. **e)** The matrices indicate the average communicability between the 4 communities obtained at $t = 1$ TR in panel a. **f)** Robustness of community detection. The plot represents the alignment of the communities for two subsets of 25% of the 77 subjects. Each plotted dot represents the coparticipation index that is a matrix element in Fig. 7a for $t = 1$ TR. **g)** Pearson correlation coefficient between the MOU-EC of the 77 subjects, between the mean MOU-EC over each subject subset and of the community coparticipation values (100 repetitions using randomly 25% of the 77 subjects as in panel a, possibly with overlap).

preserves the distribution of input and output strengths over each ROI, see Eq. (8) for details.

- The ring surrogate in Fig. 6c (left matrix) reorganizes the input connections for each ROI to promote local connectivity with a ring topology determined by the index of the ROIs. In this arbitrary topology, distant ROIs are not directly connected.
- The shortened ring in Fig. 6c (right matrix) is similar to the previous ring surrogate, but with pooling every 3 input connections, resulting in lower density (by a factor 3).

In each case, the shuffling of the original estimate is performed for each subject and the average over subjects is then calculated. Importantly, these surrogates all destroy parts of the statistics of the original weight distribution in the estimated A in a specific manner while preserving others. They all preserve the total weight in A, which is the 1st-order moment of the weight distribution, and leave the diagonal empty. For example, the random and ring surrogates both preserve the connectivity density (1st-order of the overall distribution for the binarized weight matrix) as they topologically reallocate weights from connection to connection in a one-by-one mapping, but only the ring surrogate preserves the original sum of input weights for each ROI. This is summarized in Table 2, where the mean input and output weight per ROI, which is the first order of the weight distribution "projected" in one dimension of the weight matrix. Note that each surrogate also destroys

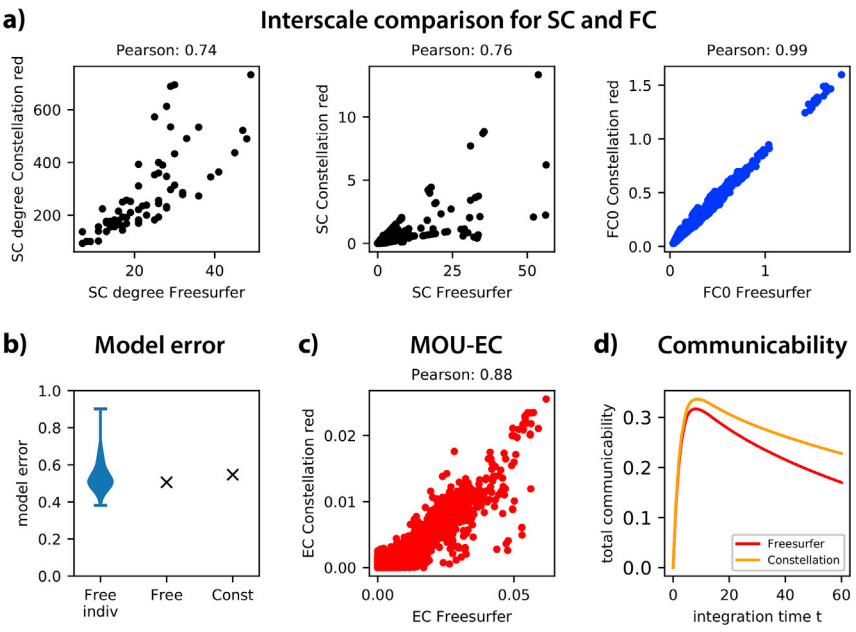

Fig. 8. Comparison of communicability for two spatial resolutions, with the Desikan and Constellation parcellations. In these plots the matrix values for Constellation with 237 ROIs are summed to reduce the matrix to the 68 ROIs of Desikan. **a)** Comparison of average SC degrees, SC values and FC values over subjects between the two parcellations. In the left plot, each black dot represents an ROI. In the middle and right plots each black/blue dot represents a link (pair of ROIs). **b)** Comparison of the model error for each subject (blue distribution) with the model error for the subject-average Desikan and Constellation models. **c)** Same as panel a for MOU-EC. **d)** Total communicability for the two parcellations.

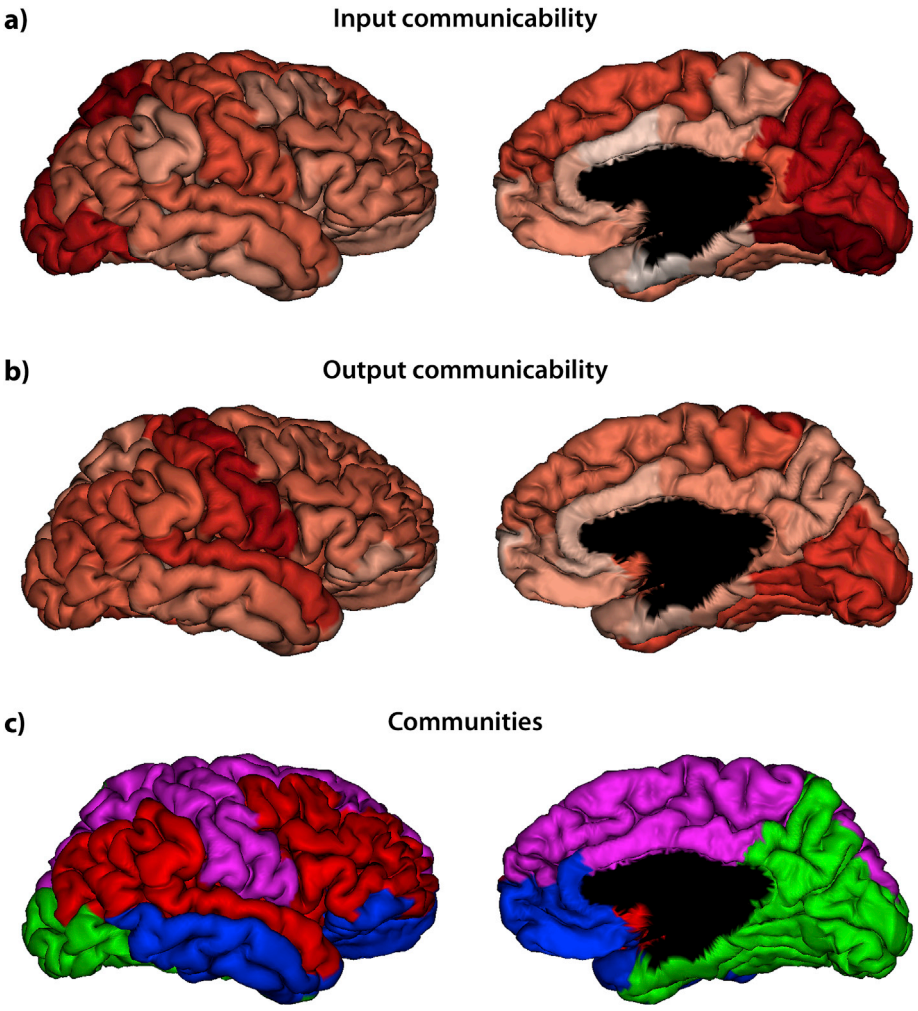

Fig. 9. Summary of results. a) Mapping of the input communicability on the cortical surface (lateral and medial views of the right hemisphere). Darker red corresponds to higher value. **b**) Same as panel a for the output communicability. **c**) Mapping of the 4 communicability-based communities at $t = 1$ TR in Fig. 7a on the cortical surface. Each color represents a community.

the second-order statistics, corresponding to the joint distribution of weights for pairs of ROIs.

The random surrogate (dark blue curve) exhibits a smaller values for $\mathscr{S}^{\mathscr{E}}$ and a homogenization slightly after 20 TR, but at a lower asymptotic value for $\mathscr{D}^{\mathscr{E}}$. The ring surrogate (dark cyan curve) destroys the local loops and clusters, which decreases $\mathscr{S}^{\mathscr{E}}$ even more strongly than for the random surrogate. In our previous theoretical study, we used ring lattice to study how communicability captures the small-worldness in networks, which corresponds to a quick stabilization of $\mathscr{D}^{\mathscr{E}}$ compared to the timescale of $\mathscr{S}^{\mathscr{E}}$ [11, Fig. 6]. Here the estimated MOU-EC exhibits a profile for $\mathscr{D}^{\mathscr{E}}$ that is much closer to the random surrogate than the ring lattice, indicating that the fluctuating activity quickly propagates throughout the whole network. Because both surrogates have the same density and individual weights, this suggests a specific internal organization for the estimated EC, related to the multiple loops and resulting in a strong network effect.

For the short ring surrogate (light cyan curve), the main difference concerns the much slower homogenization for $\mathscr{D}^{\mathscr{E}}$. This arises because shortest paths between ROIs are much longer for the short ring (light cyan curve) than the ring surrogate (dark cyan curve). This shows that the mean weight per ROI is not the relevant feature to understand the propagation of activity in the network.

Last, the null model (gray curve) also has a weaker $\mathscr{S}^{\mathscr{E}}$, but more interesting is the flat curve for $\mathscr{D}^{\mathscr{E}}$. This illustrates the already-homogenized (fully-connected) network for the surrogate obtained by randomizing the second order statistics of the connectivity. This property is the reason for its use as a baseline when performing community detection based on communicability.

To recapitulate, the comparison of those descriptors for the estimated MOU-EC with the surrogates —each specifically destroying part of the weight structure— gives insight about how close or distant the brain network dynamics are with respect to the corresponding stereotypical models. The dark red bars in Fig. 6d indicate statistical difference between the model (in red) and the 4 surrogates with p-value < 0.001 (uncorrected). For $\mathscr{S}^{\mathscr{E}}$, it concerns late integration times when the global network feedback builds up. For $\mathscr{D}^{\mathscr{E}}$, the homogenization saturates at a high value during early integration times (and faster than the short ring surrogate), suggesting a distinct detailed structure of the estimated MOU-EC as compared to the surrogates. A possible explanation is the existence of modules [11, Fig. 7], which we investigate now.

3.5. Functional communities in brain network and information integration

The high saturating value of $\mathscr{D}^{\mathscr{E}}$ in Fig. 3d is also reminiscent of hierarchical networks consisting of several modules that have rather strong coupling between them, for which the diversity stabilizes early when the total communicability is still large and close to its peak [11, see Fig. 7 there]. To further examine this aspect, we perform a community analysis to reveal the communication between ROI groups over time. In essence, communicability is compared to that obtained with the null connectivity model in gray in Fig. 6. ROIs with greater reciprocal communicability compared to the null model are grouped into communities, yielding the coparticipation matrices in Fig. 7a. These matrices measure the robustness of the communities across subjects: Well-defined correspond to dark squares on the diagonal (after reordering the ROIs), whereas weak associations of ROIs appear in lighter gray. The 4 communities correspond to observed of resting-state networks (Damoiseaux et al., 2006; van den Heuvel and Hulshoff Pol, 2010):

- insularo-temporal and lateral frontal ROIs: CMF, RMF, POPE, PTRI, SMAR, IP, BSTS, ST, MT, TT, INS;
- visual ROIs, precuneus and medial ROIs close to the hippocampus: CUN, PCAL, LING, LOCC, FUS, PARH, ENT, ISTC, PCUN;
- lower frontal and temporal ROIs plus a cingulate ROI: LOF, MOF, PORB, RAC, FP, IT, TP;
- sensorimotor ROIs and ROIs from the default-mode network: PREC, PARC, PSTC, CAC, PC, SF, SP;

in the order of the diagonal blocks from the bottom left to the top right in Fig. 7a with $t = 1$ TR. All communities are symmetric with the two homotopic ROIs in both hemispheres. The full name regions can be found in Table 1.

We firstly compare the community matrices for dynamic communicability with the same algorithm applied on FC and SC, as classically performed. The resulting community matrices in Fig. 7c and d (left panel) are distinct from those obtained from communicability in several aspects. FC-based communities are less evident (with darker pixels on average), suggesting that even the strong overall correlations between ROIs do not adequately determine the functional communities. This comes for a large part because FC is a full matrix. We quantify the similarity between the community structures using the Pearson correlation on the vectorized coparticipation matrices in Fig. 7a-c-d. For communicability at $t = 1$ TR, this gives a Pearson correlation of 0.09 with the FC-based communities. In comparison we obtain 0.12 between SC- and FC-based communities. SC-based communities are more similar to the flow-based communities, with a Pearson of 0.54 between the coparticipation matrices. This confirms that the correlation observed between input communicability and SC at the ROI level in Fig. 5 also applies to communities at the level of groups of ROIs, at least to some extent. However, in each of the 4 groups, ROIs from distinct hemisphere are separated. This underlines the importance of the estimated MOU-EC weights, which give a different community structure compared to SC in spite of the same topology. The right matrix in Fig. 7c displays the pairwise matching indices calculated for the (binarized) SC. The matching index (Wasserman and Faust, 1994) quantifies the fraction of common neighbors two ROIs share and is thus often considered as a measure of "functional similarity". However, the matching index also leaves the two hemispheres rather disconnected.

Another advantage of our approach is the quantitative description of the community merging over time, as illustrated by the distributions of coparticipation indices in Fig. 7d. The communities are still differentiated at $t \leq 10$ TR in Fig. 7a, but all of them except for the third one unite at $t = 20$ TR and they become a single community at $t = 40$ TR. The average communicability between the communities in Fig. 7e confirms this global pattern: It suggests that information is first integrated somehow independently within distinct communities, then is broadcasted to the whole network during the homogenization phase. These two modes of information integration are reminiscent of synchronization in networks for distinct values of the global coupling (Zhou and Kurths, 2006; Gómez-Gardeñes et al., 2010), but it is important to note that they are supported by the same dynamical regime in our case; they simply occur at different timescales within the network response.

We verify the robustness of the community detection by performing the same community detection with two subsets of 25% of the 77 subjects. The left plot of Fig. 7f shows the correspondence between the coparticipation indices (matrix elements in Fig. 7f) for two subsets. From this we calculate the Pearson correlation coefficient to evaluate the alignment of the communities, which corresponds to 0.9 (green distribution in the right of Fig. 7g for 100 repetitions). This can be explained because the mean MOU-EC matrices over the subjects in each subset have a very similar structure (orange distribution), even though individual MOU-EC are more moderately aligned (blue distribution). Therefore, averaging over about 20 subjects reduces the subject variability, as well as noise related to the fMRI measurements.

3.6. Comparison of BOLD dynamics at different scales

Finally, we compare communicability between two parcellations to verify whether communicability corresponds to similar dynamics when changing scale. The Constellation parcellation is a refinement of the

Desikan parcellation based on the anatomical fibers, dividing each of the original 68 ROIs into 3 to 5 new ROIs to obtain 237 ROIs with increased homogeneous SC within each ROI (Lefranc et al., 2016). Although not identical, the reduced SC is thus very similar across the parcellations in Fig. 8a. The two FC matrices show perfect correspondence. Here we focus on an average model over subjects for MOU-EC, unlike the individual models used until now. The model can be satisfactorily fitted to the average FC0 and FC1 matrices (see the model error in Fig. 8b). As a sanity check, we verify that the average of individual MOU-EC matrices correlates with the MOU-EC of the average model with a Pearson of 0.56 (not shown), which is similar to the mean Pearson correlation between individual MOU-EC (blue distribution in Fig. 8b). The comparison between the average models of the two parcellations in Fig. 8c gives a Pearson correlation of 0.88, with p-value $\ll 10^{-10}$. The time constants τ are very close, 2.52 for Desikan and 2.53 for Constellation. With this we evaluate the total communicability as a proxy for the global network dynamics and find similar curves (Fig. 8d). These results indicate that consistent information can be obtained across scales, but we leave a deeper study for future work.

4. Discussion

The present paper has introduced a network-oriented analysis of brain connectivity obtained from fMRI data, applying our recently-proposed formalism (Gilson et al., 2018). It demonstrates its flexibility in providing information at both local (single connections or ROIs) and global levels, allowing for a comprehensive description of the network going beyond a link-specific analysis. The pairwise interactions across time determined by the network dynamics are described by a family of matrices that incorporate network effects. Our results stress the importance of taking time into account to characterize the brain communication in order to describe how "information" —here measured via the propagation of BOLD signals— is integrated in the network. Recall that the scope of our approach is broader and other dynamic network models than MOU-EC can be used. In any case, we advocate for preserving the consistency of the analysis from estimation to interpretation, which is a strength compared to previous studies.

The results are summarized as plots on the cortical surface in Fig. 9. At the local scale, we have explored the functional roles of ROIs over time, e.g. broadcasters or listeners (Fig. 4a), which provides complementary information to FC and SC (Fig. 5). For instance, we have found that anatomical hub ROIs —precuneus, superior parietal and superior frontal cortex (van den Heuvel et al., 2012; Sporns, 2013)— are listeners that globally integrate information from other ROIs in the resting state, but without broadcasting much. During visual and memory tasks, they may become selective broadcasters to specific target ROIs (Senden et al., 2018). Previous studies have shown that the precuneus also acts as a selective integrator during memory and cognitive flexibility tasks (Vatansever et al., 2015, 2017). It remains to be explored with diverse tasks how this gating of input/output information is implemented by high-level ROIs, which can be related to the theory of the global workspace (Dehaene and Naccache, 2001).

At the global scale, the estimated BOLD dynamics exhibit a peak in the network response between 5 and 12 TR (Fig. 3c), while the maximum homogenization of dynamic communicability is achieved around 15 TR. This corresponds to community merging between 10 and 20 TR (Fig. 7a–b). These results speak to a multistage integration of information implemented by the cortical network —first locally within the communities, then globally. Here these two modes emerge as a natural consequence of the timescale separation due to information propagation within the network. In contrast, previous studies could only identify such modes by "artificially" setting the network into two very different dynamical states: either weakly or strongly synchronized (Zhou and Kurths, 2006; Gómez-Gardeñes et al., 2010). This flexibility may be interesting to quantify the notion of integration in networks that has attracted much attention, in particular in neuroscience (Tononi et al., 1994, 1998; Dehaene and Naccache, 2001; Deco et al., 2015; Zamora-López et al., 2016). Variability across subjects has not been explored here, but is of interest and will be studied in future work.

4.1. Model-based network descriptors for whole-brain dynamics

Our formalism opens a new dynamical perspective to interpret fMRI data, as compared to more "static" approaches using network theory that focused on FC or SC (van den Heuvel et al., 2012; Sporns, 2013). The BOLD signals obtained from fMRI are "projected" on the model parameters. MOU-EC acts as a transition matrix, measuring the propagation of fMRI (fluctuating) activity across brain areas. In addition, the input properties are described via their (co)variance matrix Σ. As an example, FC-based analysis can be considered as a "projection" of BOLD signals on a graphical model, where the successive levels of BOLD activation (for all ROIs) are considered as i.i.d. variables over time. Likewise, sliding-window FC measures are typically considered as a pool of measures with no intrinsic temporal structure (Khambhati et al., 2018; Thompson et al., 2017; Avena-Koenigsberger et al., 2017), which has also been used in other fields such as epidemic spreading (Chen et al., 2016). Other alternatives to define states and transitions between them has used clustering techniques on the instantaneous phases obtained from the Hilbert transform (Cabral et al., 2017) or HMMs to generate BOLD activation levels (Vidaurre et al., 2018). Although these approaches may be used to describe time-dependent interactions between ROIs, they do not capture the propagating nature of the BOLD signals, nor the network effect induced by these interactions. In addition, our approach conceptually differs from previous network studies that applied various types of nodal dynamics —such as Kuramoto oscillators and random walks— to static networks in order to reveal the properties of their complex topologies (Arenas et al., 2006; Boccaletti et al., 2007; Rosvall and Bergstrom, 2008).

Importantly, the general concept of our dynamics-oriented network analysis is not tied to a specific model for whole-brain activity. The multivariate measure of communicability can be derived for other dynamic models provided their Green function is known or can be numerically evaluated, like the linearized DCM used for resting-state fMRI data (Friston et al., 2014; Frässle et al., 2017; Razi et al., 2017), the multivariate autoregressive process (Messé et al., 2014) or other elaborate models that can be linearized (Breakspear, 2017; Schmidt et al., 2018). This leads to a revised formulation for Eq. (5). Nonetheless, a network analysis of the underlying connectivity —EC as discussed in a recent publication (Park et al., 2018) or equivalent— only provides a snapshot view on the dynamics. Our results show that it corresponds to the initial integration time and that a more complete viewpoint is obtained when taking time into account (e.g. community merging). Other measures of directed connectivity can be used as matrix A to calculate communicability, such as Granger causality analysis (Yan and He, 2011; Seth et al., 2013; Brovelli et al., 2015). However, this requires the choice of a leakage time constant τ in Eq. (1). In our case the knowledge about τ comes from the MOU-EC estimation procedure, which gives the full Jacobian J. Ensuring consistency from model estimation to interpretation is an important point in our opinion.

The presented framework allows for the analysis of connectivity at various scales. At the global level, the total communicability $\mathscr{T}^{\mathscr{C}}$ measures how the inputs circulate over the integration time via MOU-EC. The stabilization of $\mathscr{T}^{\mathscr{C}}$ indicates the temporal horizon when the network interactions become most homogeneous. At the local scale, we have explored the functional roles of ROIs over time, e.g. broadcasters or listeners (Fig. 4a), which provides complementary information to FC and SC (Fig. 5). At an intermediate level, community detection uncovers the functional organization of ROIs (Fig. 7a). For the studied dataset, MOU-EC determines functional communities in a much more accurate manner than FC (Fig. 7c). This is an important point to analyze task-dependent communities, which is not possible using SC.

Another interesting aspect of our formalism is the quantitative comparison between network dynamics. With surrogate networks such as ring lattices or random networks, it reveals the properties of the estimated MOU-EC (Fig. 6). Here we have compared global measures: the total communicability $\mathscr{S}^{\mathscr{C}}$ is the sum of all interactions at a given time and the diversity $\mathscr{D}^{\mathscr{C}}$ reflects their heterogeneity within the network. These time-dependent measures correspond to curves that are more or less distant, providing a metric to compare the data with specific topologies. Likewise, the comparison of the MOU-EC for two parcellations using communicability demonstrates a consistency across scales (Fig. 8).

In addition to the MOU-EC matrix A and the leakage related to τ, the MOU dynamics is determined by the properties of its fluctuating inputs (in purple in Fig. 3a), related to their (co)variance matrix Σ. The Σ estimated from data is task-dependent and off-diagonal elements may be tuned to model ROIs that experience cross-correlated noise (Gilson et al., 2018b). To incorporate the effect of Σ in the network dynamics, another family of time-dependent matrices can be defined, which was name the flow (Gilson et al., 2018). In fact, dynamic communicability is a particular case of the flow for homogeneous input statistics ($\Sigma_{ii} = 1$ for all ROIs). Practically, the difference between the two measure is the following: Dynamic communicability describes how standard input fluctuations propagate throughout the network connectivity, whereas the flow quantifies the propagation of fluctuating activity for the brain dynamical "state" estimated over the whole session. Communicability is thus appropriate to study the effect of network connectivity alone, whereas the flow is better suited when Σ depends on the subject's condition for as was shown for movie viewing versus rest (Gilson et al., 2018b).

4.2. Advantages and limitations of MOU-EC

The present application of dynamic communicability relies on the MOU process for the connectivity estimation. The MOU network corresponds to a non-conservative and stationary propagation of fluctuating activity, which was used to study network complexity (Tononi et al., 1994; Galán, 2008; Barnett et al., 2009; Zamora-López et al., 2016). The MOU process has also been used in many other scientific disciplines (Vasicek, 1977; Britton and Neal, 2010; Andersson and Lindenstrand, 2011), in particular for time-series analysis (Lütkepohl, 2005). The viewpoint taken on the MOU process is a "noise"-diffusion network where fluctuating activity propagates, EC defining the input-output mapping (Gilson, 2018). Moreover, MOU-EC has been demonstrated to provide robust biomarkers for subject or task identification from BOLD signals (Pallarés et al., 2018).

When the MOU-EC estimation was developed, it aimed to solve the trade-off between robust estimation and application to large brain network (70 + ROIs) by using linear dynamics (Gilson et al., 2016). As mentioned earlier, the EC terminology was borrowed from the DCM literature because of the model-based aspect (Friston, 2011). Several points were identified a few years ago when discussing the concepts behind effective connectivity and Granger causality analysis (Valdes--Sosa et al., 2011), in particular subsampling related to the low time resolution of BOLD signals and the hemodynamic response function. Because the MOU works in continuous time, it deals with the subsampling associated with the low temporal resolution of the BOLD signals (Gilson et al., 2016). This contrasts with estimation methods relying on the discrete-time multivariate autoregressive process that may be sensitive to subsampling for BOLD signals (Seth et al., 2013). The absence of hemodynamics in MOU-EC is a crucial difference with DCM. An in-depth comparison between the two methods is left to future work and readers interested in whole-brain analysis involving hemodynamics are referred to recent extensions of the DCM (Frässle et al., 2017; Razi et al., 2017). A related point concerns the single time constant τ for all ROIs chosen for each subject, which was motivated from the analyzed data. Further study —possibly with more datasets— is necessary to explore the possibility of finessing the model with ROI-specific τ. Recall also that any interpretation of BOLD in term of brain communication relies on the assumption that changes in neuronal activity are reliably reflected in the BOLD signals, which is under debate (Goense et al., 2012; Matsui et al., 2019; He et al., 2018).

The model optimization performed here ensures that the matrix Σ remains diagonal, which has consequences on the estimated MOU-EC. This effect was observed in a previous study for task-evoked activity (Gilson et al., 2018b), but not consistently explored so far. In the present version the MOU-EC does not incorporate common inputs, which means that the A estimates may compensate with stronger weights to explain the observed correlations in FC. However, there is no whole-brain dynamic model that has quantitatively addressed this difficult issue in depth so far in our knowledge.

Acknowledgements

This work has been supported by the European Union's Horizon 2020 research and innovation programme under Grant Agreement No. 720270 (Human Brain Project SGA1) and No. 785907 (Human Brain Project SGA2), concerning MG, GZL, NEK and GD. MG also acknowledges funding from the Marie Skłodowska-Curie Action (Grant H2020-MSCA-656547) of the European Commission. GD also acknowledges funding from the Spanish Ministry Research Project PSI2016-75688-P (AEI/FEDER) and by the and by the Catalan Research Group Support 2017 SGR 1545. NEK acknowledges support from the "MOVE-IN Louvain" fellowship co-funded by the Marie Skłodowska-Curie Action of the European Commission.

The "CONNECT/Archi Database" is the property of the CEA I2BM NeuroSpin centre and was designed under the supervision of Dr Cyril Poupon and Dr Jean-François Mangin. It was funded by the Federative Research Institute 49, by the HIPPIP European grant, and the European CONNECT project (http://www.brain-connect.eu). Acquisitions were performed by the scientists involved in the Multi-scale Brain Architecture research program of NeuroSpin and by the staff of the UNIACT Laboratory of NeuroSpin (headed by Dr Lucie Hertz-Pannier), under the ethical approval CPP100002/CPP100022 (principal investigator Dr Denis Le Bihan). Access to the database can be requested from cyril.poupon@cea.fr.

References

Albert, R., Barabási, A.-L., 2002. Statistical mechanics of complex networks. Rev. Mod. Phys. 74, 47–97. https://doi.org/10.1103/RevModPhys.74.47. URL.

Andersson, P., Lindenstrand, D., 2011. A stochastic SIS epidemic with demography: initial stages and time to extinction. J. Math. Biol. 62, 333–348. https://doi.org/10.1007/s00285-010-0336-x.

Andreotti, J., Jann, K., Melie-Garcia, L., Giezendanner, S., Abela, E., Wiest, R., Dierks, T., Federspiel, A., 2014. Validation of network communicability metrics for the analysis of brain structural networks. PLoS One 9, e115503. https://doi.org/10.1371/journal.pone.0115503.

Arenas, A., Díaz-Guilera, A., Pérez-Vicente, C.J., 2006. Synchronization reveals topological scales in complex networks. Phys. Rev. Lett. 96, 114102. https://doi.org/10.1103/PhysRevLett.96.114102.

Arrigo, F., Benzi, M., 2016. Updating and downdating techniques for optimizing network communicability. SIAM J. Sci. Comput. 38, B25–B49. https://doi.org/10.1137/140991923.

Assaf, Y., Alexander, D.C., Jones, D.K., Bizzi, A., Behrens, T.E.J., Clark, C.A., Cohen, Y., Dyrby, T.B., Huppi, P.S., Knoesche, T.R., Lebihan, D., Parker, G.J.M., Poupon, C., , CONNECT consortium, Anaby, D., Anwander, A., Bar, L., Barazany, D., Blumenfeld-Katzir, T., De-Santis, S., Duclap, D., Figini, M., Fischi, E., Guevara, P., Hubbard, P., Hofstetter, S., Jbabdi, S., Kunz, N., Lazeyras, F., Lebois, A., Liptrot, M.G., Lundell, H., Mangin, J.-F., Dominguez, D.M., Morozov, D., Schreiber, J., Seunarine, K., Nava, S., Poupon, C., Riffert, T., Sasson, E., Schmitt, B., Shemesh, N., Sotiropoulos, S.N., Tavor, I., Zhang, H.G., Zhou, F.-L., 2013. The CONNECT project: combining macro- and micro-structure. Neuroimage 80, 273–282. https://doi.org/10.1016/j.neuroimage.2013.05.055.

Avena-Koenigsberger, A., Misic, B., Sporns, O., 2017. Communication dynamics in complex brain networks. Nat. Rev. Neurosci. 19, 17–33. https://doi.org/10.1038/nrn.2017.149.

Baars, B., 1988. A Cognitive Theory of Consciousness. Cambridge University Press.

Baars, B.J., 2002. The conscious access hypothesis: origins and recent evidence. Trends Cogn. Sci. 6, 47–52.

Bang-Jensen, J., Gutin, G., 2009. Digraphs: Theory, Algorithms and Applications, second ed. Springer-Verlag.
Barnett, L., Buckley, C.L., Bullock, S., 2009. Neural complexity and structural connectivity. Phys. Rev. E - Stat. Nonlinear Soft Matter Phys. 79, 051914. https://doi.org/10.1103/PhysRevE.79.051914.
Barrat, A., Barthélemy, M., Pastor-Satorras, R., Vespignani, A., 2004. The architecture of complex weighted networks. Proc. Natl. Acad. Sci. U. S. A. 101, 3747–3752. https://doi.org/10.1073/pnas.0400087101.
Benzi, M., Klymko, C., 2013. Total communicability as a centrality measure. J. Complex Networks 1, 124–149. https://doi.org/10.1093/comnet/cnt007.
Bettinardi, R.G., Deco, G., Karlaftis, V.M., Van Hartevelt, T.J., Fernandes, H.M., Kourtzi, Z., Kringelbach, M.L., Zamora-López, G., 2017. How structure sculpts function: unveiling the contribution of anatomical connectivity to the brain's spontaneous correlation structure. Chaos 27, 047409. https://doi.org/10.1063/1.4980099.
Boccaletti, S., Ivanchenko, M., Latora, V., Pluchino, A., Rapisarda, A., 2007. Detecting complex network modularity by dynamical clustering. Phys. Rev. E - Stat. Nonlinear Soft Matter Phys. 75, 045102. https://doi.org/10.1103/PhysRevE.75.045102.
Breakspear, M., 2017. Dynamic models of large-scale brain activity. Nat. Neurosci. 20, 340–352. https://doi.org/10.1038/nn.4497.
Britton, T., Neal, P., 2010. The time to extinction for a stochastic SIS-household-epidemic model. J. Math. Biol. 61, 763–779. https://doi.org/10.1007/s00285-009-0320-5.
Brovelli, A., Chicharro, D., Badier, J.-M., Wang, H., Jirsa, V., 2015. Characterization of cortical networks and corticocortical functional connectivity mediating arbitrary visuomotor mapping. J. Neurosci. 35, 12643–12658. https://doi.org/10.1523/JNEUROSCI.4892-14.2015.
Bzdok, D., Varoquaux, G., Grisel, O., Eickenberg, M., Poupon, C., Thirion, B., 2016. Formal models of the network co-occurrence underlying mental operations. PLoS Comput. Biol. 12, e1004994. https://doi.org/10.1371/journal.pcbi.1004994.
Cabral, J., Hugues, E., Sporns, O., Deco, G., 2011. Role of local network oscillations in resting-state functional connectivity. Neuroimage 57, 130–139.
Cabral, J., Vidaurre, D., Marques, P., Magalhães, R., Silva Moreira, P., Miguel Soares, J., Deco, G., Sousa, N., Kringelbach, M.L., 2017. Cognitive performance in healthy older adults relates to spontaneous switching between states of functional connectivity during rest. Sci. Rep. 7, 5135. https://doi.org/10.1038/s41598-017-05425-7.
Chang, L., Gianaros, P., Manuck, S., Krishnan, A., Wager, T., 2015. A sensitive and specific neural signature for picture-induced negative affect. PLoS Biol. 13, e1002180.
Chen, I., Benzi, M., Chang, H.H., Hertzberg, V.S., 2016. Dynamic communicability and epidemic spread: a case study on an empirical dynamic contact network. J. Complex Networks 5, 274–302. https://doi.org/10.1093/comnet/cnw017.
Ciuciu, P., Abry, P., He, B.J., 2014. Interplay between functional connectivity and scale-free dynamics in intrinsic fMRI networks. Neuroimage 95, 248–263.
Damoiseaux, J.S., Rombouts, S.A.R.B., Barkhof, F., Scheltens, P., Stam, C.J., Smith, S.M., Beckmann, C.F., 2006. Consistent resting-state networks across healthy subjects. Proc. Natl. Acad. Sci. U. S. A. 103, 13848–13853. https://doi.org/10.1073/pnas.0601417103.
Deco, G., Kringelbach, M.L., 2014. Great expectations: using whole-brain computational connectomics for understanding neuropsychiatric disorders. Neuron 84, 892–905. https://doi.org/10.1016/j.neuron.2014.08.034.
Deco, G., Jirsa, V., McIntosh, A., 2011. Emerging concepts for the dynamical organization of resting-state activity in the brain. Nat. Rev. Neurosci. 12, 43–56.
Deco, G., Ponce-Alvarez, A., Mantini, D., Romani, G., Hagmann, P., Corbetta, M., 2013. Resting-state functional connectivity emerges from structurally and dynamically shaped slow linear fluctuations. J. Neurosci. 33, 11239–11252.
Deco, G., Tononi, G., Boly, M., Kringelbach, M.L., 2015. Rethinking segregation and integration: contributions of whole-brain modelling. Nat. Rev. Neurosci. 16, 430–439. https://doi.org/10.1038/nrn3963.
Dehaene, S., Naccache, L., 2001. Towards a cognitive neuroscience of consciousness: basic evidence and a workspace framework. Cognition 79, 1–37.
Descoteaux, M., Angelino, E., Fitzgibbons, S., Deriche, R., 2007. Regularized, fast, and robust analytical Q-ball imaging. Magn. Reson. Med. 58, 497–510. https://doi.org/10.1002/mrm.21277.
Desikan, R.S., Ségonne, F., Fischl, B., Quinn, B.T., Dickerson, B.C., Blacker, D., Buckner, R.L., Dale, A.M., Maguire, R.P., Hyman, B.T., Albert, M.S., Killiany, R.J., 2006. An automated labeling system for subdividing the human cerebral cortex on mri scans into gyral based regions of interest. Neuroimage 31, 968–980. https://doi.org/10.1016/j.neuroimage.2006.01.021.
Duclap, D., Lebois, A., Schmitt, B., Riff, O., Guevara, P., Marrakchi-Kacem, L., Brion, V., Poupon, F., Mangin, J.-F., Poupon, C., 2012. Connectomist-2.0: a novel diffusion analysis toolbox for BrainVISA. In: 29th ESMRMB. Lisbone, Portugal.
Duclap, D., Schmitt, B., Lebois, A., Guevara, P., Zhang, H., Longo Dos Santos, C., Le Bihan, D., Mangin, J.-F., Poupon, C., 2013. Towards a super-resolution CONNECT/ARCHI atlas of the white matter connectivity. In: Proc Int Soc Magn Reson Med 21th Annual Meeting, p. 3153.
Estrada, E., 2013. Communicability in temporal networks. Phys. Rev. E - Stat. Nonlinear Soft Matter Phys. 88, 042811. https://doi.org/10.1103/PhysRevE.88.042811.
Estrada, E., Hatano, N., 2008. Communicability in complex networks. Phys. Rev. E - Stat. Nonlinear Soft Matter Phys. 77, 036111. https://doi.org/10.1103/PhysRevE.77.036111.
Fair, D.A., Dosenbach, N.U.F., Church, J.A., Cohen, A.L., Brahmbhatt, S., Miezin, F.M., Barch, D.M., Raichle, M.E., Petersen, S.E., Schlaggar, B.L., 2007. Development of distinct control networks through segregation and integration. Proc. Natl. Acad. Sci. U. S. A. 104, 13507–13512. https://doi.org/10.1073/pnas.0705843104.
Fischl, B., Sereno, M.I., Dale, A.M., 1999. Cortical surface-based analysis. II: inflation, flattening, and a surface-based coordinate system. Neuroimage 9, 195–207. https://doi.org/10.1006/nimg.1998.0396.
Fransson, P., Schiffler, B.C., Thompson, W.H., 2018. Brain network segregation and integration during an epoch-related working memory fmri experiment. Neuroimage 178, 147–161. https://doi.org/10.1016/j.neuroimage.2018.05.040.
Frässle, S., Lomakina, E.I., Razi, A., Friston, K.J., Buhmann, J.M., Stephan, K.E., 2017. Regression DCM for fMRI. Neuroimage 155, 406–421. https://doi.org/10.1016/j.neuroimage.2017.02.090.
Friston, K., 2011. Functional and effective connectivity: a review. Brain Connect. 1, 8.
Friston, K.J., Kahan, J., Biswal, B., Razi, A., 2014. A DCM for resting state fMRI. Neuroimage 94, 396–407. https://doi.org/10.1016/j.neuroimage.2013.12.009.
Galán, R.F., 2008. On how network architecture determines the dominant patterns of spontaneous neural activity. PLoS One 3, e2148. https://doi.org/10.1371/journal.pone.0002148.
Gilson, M., 2018. Analysis of Fmri Data Using Noise-Diffusion Network Models: a New Covariance-Coding Perspective. Biological Cybernetics 112, 153–161. https://doi.org/10.1007/s00422-017-0741-y.
Gilson, M., Kouvaris, N.E., Deco, G., Zamora-Lopez, G., 2018. Dynamic communicability and flow to describe complex network dynamics with linear feedback. Phys. Rev. 97, 052301.
Gilson, M., Moreno-Bote, R., Ponce-Alvarez, A., Ritter, P., Deco, G., 2016. Estimation of directed effective connectivity from fmri functional connectivity hints at asymmetries of cortical connectome. PLoS Comput. Biol. 12, e1004762.
Gilson, M., Deco, G., Friston, K., Hagmann, P., Mantini, D., Betti, V., Romani, G.L., Corbetta, M., 2018. Effective connectivity inferred from fmri transition dynamics during movie viewing points to a balanced reconfiguration of cortical interactions. Neuroimage 180, 534–546. https://doi.org/10.1016/j.neuroimage.2017.09.061.
Goense, J., Whittingstall, K., Logothetis, N.K., 2012. Neural and bold responses across the brain. Wiley Interdiscip. Rev. Cogn. Sci. 3, 75–86. https://doi.org/10.1002/wcs.153.
Gómez-Gardeñes, J., Zamora-López, G., Moreno, Y., Arenas, A., 2010. From modular to centralized organization of synchronization in functional areas of the cat cerebral cortex. PLoS One 5, e12313. https://doi.org/10.1371/journal.pone.0012313.
Gorgolewski, K., Burns, C.D., Madison, C., Clark, D., Halchenko, Y.O., Waskom, M.L., Ghosh, S.S., 2011. Nipype: a flexible, lightweight and extensible neuroimaging data processing framework in python. Front. Neuroinf. 5, 13. https://doi.org/10.3389/fninf.2011.00013.
Guevara, P., Duclap, D., Marrakchi-Kacem, L., Rivière, D., Cointepas, Y., Poupon, C., Mangin, F.-F., 2011. Accurate tractography propagation mask using T1-weighted data rather than FA. Proc. Intl. Soc. Mag. Reson. Med 19, 2011.
He, B.J., 2011. Scale-free properties of the functional magnetic resonance imaging signal during rest and task. J. Neurosci. 31, 13786–13795.
He, Y., Wang, M., Chen, X., Pohmann, R., Polimeni, J.R., Scheffler, K., Rosen, B.R., Kleinfeld, D., Yu, X., 2018. Ultra-slow single-vessel bold and cbv-based fmri spatiotemporal dynamics and their correlation with neuronal intracellular calcium signals. Neuron 97, 925–939. https://doi.org/10.1016/j.neuron.2018.01.025.
Hutchison, R.M., Womelsdorf, T., Allen, E.A., Bandettini, P.A., Calhoun, V.D., Corbetta, M., Della Penna, S., Duyn, J.H., Glover, G.H., Gonzalez-Castillo, J., Handwerker, D.A., Keilholz, S., Kiviniemi, V., Leopold, D.A., de Pasquale, F., Sporns, O., Walter, M., Chang, C., 2013. Dynamic functional connectivity: promise, issues, and interpretations. Neuroimage 80, 360–378. https://doi.org/10.1016/j.neuroimage.2013.05.079.
Khambhati, A.N., Sizemore, A.E., Betzel, R.F., Bassett, D.S., 2018. Modeling and interpreting mesoscale network dynamics. Neuroimage 180, 337–349. https://doi.org/10.1016/j.neuroimage.2017.06.029.
Lefranc, S., Roca, P., Perrot, M., Poupon, C., Le Bihan, D., Mangin, J.-F., Rivière, D., 2016. Groupwise connectivity-based parcellation of the whole human cortical surface using watershed-driven dimension reduction. Med. Image Anal. 30, 11–29. https://doi.org/10.1016/j.media.2016.01.003.
Lütkepohl, H., 2005. New Introduction to Multiple Time Series Analysis. Springer Science & Business Media.
Matsui, T., Murakami, T., Ohki, K., 2019. Neuronal origin of the temporal dynamics of spontaneous bold activity correlation. Cerebr. Cortex 29, 1496–1508. https://doi.org/10.1093/cercor/bhy045.
Messé, A., Rudrauf, D., Benali, H., Marrelec, G., 2014. Relating structure and function in the human brain: relative contributions of anatomy, stationary dynamics, and non-stationarities. PLoS Comput. Biol. 10, e1003530.
Mitra, A., Snyder, A.Z., Tagliazucchi, E., Laufs, H., Raichle, M., 2015. Propagated infra-slow intrinsic brain activity reorganizes across wake and slow wave sleep. Elife 4, e10781.
Newman, M.E.J., 2006. Modularity and community structure in networks. Proc. Natl. Acad. Sci. U. S. A. 103, 8577–8582. https://doi.org/10.1073/pnas.0601602103.
Nielsen, S.F.V., Schmidt, M.N., Madsen, K.H., Mørup, M., 2018. Predictive assessment of models for dynamic functional connectivity. Neuroimage 171, 116–134. https://doi.org/10.1016/j.neuroimage.2017.12.084.
Pallarés, V., Insabato, A., Sanjuán, A., Kühn, S., Mantini, D., Deco, G., Gilson, M., 2018. Extracting orthogonal subject- and condition-specific signatures from fmri data using whole-brain effective connectivity. Neuroimage 178, 238–254. https://doi.org/10.1016/j.neuroimage.2018.04.070.
Park, H.-J., Friston, K.J., Pae, C., Park, B., Razi, A., 2018. Dynamic effective connectivity in resting state fmri. Neuroimage 180, 594–608. https://doi.org/10.1016/j.neuroimage.2017.11.033.
Raemaekers, M., Schellekens, W., Petridou, N., Ramsey, N.F., 2018. Knowing left from right: asymmetric functional connectivity during resting state. Brain Struct. Funct. 223, 1909–1922. https://doi.org/10.1007/s00429-017-1604-y.
Razi, A., Seghier, M.L., Zhou, Y., McColgan, P., Zeidman, P., Park, H.-J., Sporns, O., Rees, G., Friston, K.J., 2017. Large-scale dcms for resting-state fmri. Networks Neurosci. 1, 222–241. https://doi.org/10.1162/NETN_a_00015.

Rosvall, M., Bergstrom, C.T., 2008. Maps of random walks on complex networks reveal community structure. Proc. Natl. Acad. Sci. U. S. A. 105, 1118–1123. https://doi.org/10.1073/pnas.0706851105.

Schmidt, M., Bakker, R., Hilgetag, C.C., Diesmann, M., van Albada, S.J., 2018. Multi-scale account of the network structure of macaque visual cortex. Brain Struct. Funct. 223, 1409–1435. https://doi.org/10.1007/s00429-017-1554-4.

Schröter, M.S., Spoormaker, V.I., Schorer, A., Wohlschläger, A., Czisch, M., Kochs, E.F., Zimmer, C., Hemmer, B., Schneider, G., Jordan, D., Ilg, R., 2012. Spatiotemporal reconfiguration of large-scale brain functional networks during propofol-induced loss of consciousness. J. Neurosci. 32, 12832–12840. https://doi.org/10.1523/JNEUROSCI.6046-11.2012.

Senden, M., Reuter, N., van den Heuvel, M.P., Goebel, R., Deco, G., Gilson, M., 2018. Task-related effective connectivity reveals that the cortical rich club gates cortex-wide communication. Hum. Brain Mapp. 39, 1246–1262. https://doi.org/10.1002/hbm.23913.

Senden, M., Deco, G., de Reus, M.A., Goebel, R., van den Heuvel, M.P., 2014. Rich club organization supports a diverse set of functional network configurations. Neuroimage 96, 174–182. https://doi.org/10.1016/j.neuroimage.2014.03.066.

Seth, A.K., Chorley, P., Barnett, L.C., 2013. Granger causality analysis of fmri bold signals is invariant to hemodynamic convolution but not downsampling. Neuroimage 65, 540–555. https://doi.org/10.1016/j.neuroimage.2012.09.049.

Sporns, O., 2013. Making sense of brain network data. Nat. Methods 10, 491–493.

Sporns, O., Tononi, G., Edelman, G.M., 2000. Theoretical neuroanatomy: relating anatomical and functional connectivity in graphs and cortical connection matrices. Cerebr. Cortex 10, 127–141.

Thompson, W.H., Brantefors, P., Fransson, P., 2017. From static to temporal network theory: applications to functional brain connectivity. Neurosci.-Net 1 (2), 69–99. https://doi.org/10.1162/NETN_a_00011. URL.

Tononi, G., Sporns, O., Edelman, G.M., 1994. A measure for brain complexity: relating functional segregation and integration in the nervous system. Proc. Natl. Acad. Sci. U. S. A. 91, 5033–5037.

Tononi, G., Edelman, G.M., Sporns, O., 1998. Complexity and coherency: integrating information in the brain. Trends Cogn. Sci. 2, 474–484.

Valdes-Sosa, P., Roebroeck, A., Daunizeau, J., Friston, K., 2011. Effective connectivity: influence, causality and biophysical modeling. Neuroimage 58, 339–361.

van den Heuvel, M.P., Hulshoff Pol, H.E., 2010. Exploring the brain network: a review on resting-state fmri functional connectivity. Eur. Neuropsychopharmacol. 20, 519–534. https://doi.org/10.1016/j.euroneuro.2010.03.008.

van den Heuvel, M.P., Kahn, R.S., Goñi, J., Sporns, O., 2012. High-cost, high-capacity backbone for global brain communication. Proc. Natl. Acad. Sci. U. S. A. 109, 11372–11377. https://doi.org/10.1073/pnas.1203593109.

Vasicek, O., 1977. An equilibrium characterization of the term structure. J. Financ. Econ. 5, 177–188. https://doi.org/10.1016/0304-405X(77)90016-2.

Vatansever, D., Menon, D.K., Manktelow, A.E., Sahakian, B.J., Stamatakis, E.A., 2015. Default mode dynamics for global functional integration. J. Neurosci. 35, 15254–15262. https://doi.org/10.1523/JNEUROSCI.2135-15.2015.

Vatansever, D., Menon, D.K., Stamatakis, E.A., 2017. Default mode contributions to automated information processing. Proc. Natl. Acad. Sci. U. S. A. 114, 12821–12826. https://doi.org/10.1073/pnas.1710521114.

Vidaurre, D., Abeysuriya, R., Becker, R., Quinn, A.J., Alfaro-Almagro, F., Smith, S.M., Woolrich, M.W., 2018. Discovering dynamic brain networks from big data in rest and task. Neuroimage 180, 646–656. https://doi.org/10.1016/j.neuroimage.2017.06.077.

Wasserman, S., Faust, K., 1994. Social Network Analysis. Cambridge University Press, Cambridge.

Yan, C., He, Y., 2011. Driving and driven architectures of directed small-world human brain functional networks. PLoS One 6, e23460. https://doi.org/10.1371/journal.pone.0023460.

Zamora-López, G., Zhou, C., Kurths, J., 2009. Graph analysis of cortical networks reveals complex anatomical communication substrate. Chaos 19, 015117. https://doi.org/10.1063/1.3089559.

Zamora-López, G., Chen, Y., Deco, G., Kringelbach, M.L., Zhou, C., 2016. Functional complexity emerging from anatomical constraints in the brain: the significance of network modularity and rich-clubs. Sci. Rep. 6, 38424. https://doi.org/10.1038/srep38424.

Zhou, C., Kurths, J., 2006. Hierarchical synchronization in complex networks with heterogeneous degrees. Chaos 16, 015104. https://doi.org/10.1063/1.2150381.